Finite Element Modeling of Gas-Surface Interactions in Hypersonic Flight

John Yuzhen Huang

Department of Mechanical Engineering
McGill University, Montreal
March 2022

A thesis submitted to McGill University
in partial fulfillment of the requirements for the degree of
Master of Science

Abstract

Numerical simulations of the effects of gas-surface interactions on gas composition and heat flux at the surface are of paramount importance to the design of thermal protection system of hypersonic vehicles. The present work extends the capabilities of the edge-based finite element three-dimensional all-Mach-number computational fluid dynamics (CFD) code HALO3D by the introduction of partially catalytic and finite-rate surface chemistry models.

The partially catalytic model assumes that a fraction of the impinging atoms, whose value is governed by recombination efficiencies derived from arcjet test data, recombines on the surface. Its development is validated using the test data of the Electre blunt cone from the high-enthalpy shock tunnel of the German Aerospace Center. Results are obtained for a five-species Mach 9.7 flow using an unstructured mesh that underwent several anisotropic optimization cycles through OptiGrid. The heat flux profiles for partially catalytic surfaces are in good agreement with previously published numerical solutions and experimental data.

The more accurate finite-rate surface chemistry model calculates recombination rates using surface reaction kinetics. Surface species with distinct thermodynamic properties are introduced to complement existing volume species. Three types of surface reaction mechanisms are considered: adsorption/desorption, Eley–Rideal, and Langmuir–Hinshelwood, with the reaction rate coefficients being dependent on surface properties. The spatial assembly and temporal integration of species production terms are validated by matching the transient response of a reactor with an analytical solution for a single irreversible adsorption reaction. The computation of forward and backward surface reaction rate coefficients is verified by comparing the equilibrium results of a reactor with multiple reversible surface reactions with previously published numerical solutions. Finally, a simulation with a reacting air flow around a cylinder with a catalytic silica surface is performed to demonstrate near-wall gas composition calculations using the finite-rate surface chemistry model.

This work enables HALO3D to provide accurate predictions of gas composition and heat flux at the surface for the practical design of hypersonic vehicles and constitutes a cornerstone to further code extensions that are currently underway at the McGill University CFD Laboratory, focusing on the modeling of partially ionized flows and ablation.

Résumé

Les simulations numériques modélisant les effets des interactions gaz-surface sur la composition du gaz en proche paroi et le transfert de chaleur à la surface sont d'une importance capitale lors de la conception des systèmes de protection thermique de véhicules hypersoniques. Le présent travail étend les capacités du code tridimensionnel de dynamique des fluides computationnelle (CFD) HALO3D – dont les équations de conservation de masse, quantité de mouvement, et d'énergie, sont discrétisées avec une méthode d'éléments finis (FEM) basée sur les arêtes – en introduisant les modèles de chimie de surface à catalycité partielle et à taux fini.

Le modèle de surface partiellement catalytique suppose qu'une fraction des atomes incidents, dont la valeur est régie par les efficacités de recombinaison dérivées de données d'arcjet, se recombine à la paroi. Son développement est validé à l'aide de données d'essais obtenues pour un cône émoussé appelé Electre testé dans le tunnel à haute enthalpie du Centre Aérospatial Allemand. Les résultats numériques pour cet écoulement à Mach 9,7 composé de cinq espèces chimiques sont obtenus utilisant un maillage non structuré qui a subi plusieurs cycles d'optimisation anisotrope à l'aide du logiciel OptiGrid. Les profils du flux thermique pour des surfaces partiellement catalytiques sont en bon accord avec les solutions numériques précédemment publiées et les données expérimentales.

Le modèle plus précis de chimie de surface à taux fini s'appuie sur la cinétique des réactions de surface. Des espèces de surface sont introduites pour compléter les espèces de volume existantes et trois types de mécanismes sont considérés: adsorption/désorption, Eley–Rideal et Langmuir–Hinshelwood. L'assemblage spatial et l'intégration temporelle des termes de production des espèces sont validés en faisant correspondre la réponse transitoire d'un réacteur avec une solution analytique pour une unique réaction irréversible d'adsorption. Le calcul des coefficients de vitesse dans les deux sens, direct et inverse, ont fait l'objet de comparaisons code-à-code pour un réacteur présentant de multiples réactions de surface réversibles. Enfin, une simulation d'un écoulement d'air réactif autour d'un

cylindre avec une surface catalytique en silice est réalisée pour démontrer les calculs de composition du gaz en proche paroi en utilisant le modèle de chimie de surface à taux fini.

Ce travail premet au code HALO3D de prédire la composition du gaz et flux de chaleur à la surface pour la conception pratique de véhicules hypersoniques et constitue également la pierre angulaire d'autres extensions du code qui sont en cours au Laboratoire de CFD de l'Université McGill, centrées sur la modélisation d'écoulements partiellement ionisés et le phénomène d'ablation.

Acknowledgements

I would like to express my most sincere gratitude towards my thesis supervisor, Professor Wagdi G. Habashi, for his indefatigable mentorship and generous support throughout my research. I also wish to convey my heartfelt appreciations for the invaluable guidance and insights that I received from Drs. Vincent Casseau, Song Gao, and Dario Isola throughout my work. I want to thank all the members of the McGill University CFD Laboratory for their support and friendship.

I would like to thank the Lockheed Martin Corporation, Ansys Canada, and Mitacs for funding the research through the Mitacs Accelerate grant. I also want to acknowledge Compute Canada and Calcul Québec for providing supercomputing resources for the research.

I am deeply grateful for my family and friends who have continuously encouraged and supported me in pursuing my dreams. To my parents I dedicate this thesis.

"Start where you are. Use what you have. Do what you can."

— Arthur Ashe

Table of Contents

List of Figures

List of Tables

Nomenclature

Latin symbols

a	speed of sound
A	Jacobian matrix
A_s	generic species symbol
c	volume mixture molar concentration
c_p	mixture specific heat capacities at constant pressure
c_v	mixture specific heat capacities at constant volume
C	pre-exponential coefficient
$\bar{\bar{d}}_{ij}$	viscous edge coefficients
D	mixture diffusion coefficient
e	total energy per unit mass
e_int	internal energy per unit mass
e_s	species internal energy
E_a	activation energy
E_i	set of elements sharing node i
F	fluxes
F_i	set of faces sharing node i
G_s^0	species Gibbs free energy
h_s	species specific enthalpy
$\bar{\bar{H}}$	Hessian matrix
$\bar{\bar{I}}$	identity matrix
$\vec{J}_s$	species mass flux
$k_{\mathrm{f},r}$, $k_{\mathrm{b},r}$	forward and backward reaction rate coefficients, respectively
K	mass matrix
$K_{\mathrm{c},r}$, $K_{\mathrm{a},r}$	concentration-based and activity-based equilibrium constants, respectively
K_e	set of nodes belonging to element e

K_i	set of nodes connected to node i via an element edge
$\bar{\bar{L}}$	left eigenvectors
L_i	lumped mass matrix
$\int \mathrm{d}L$	line integral
$\dot{m}_s$	species mass production rate
M	mixture molar mass
$\bar{\bar{M}}$	metric based on $\bar{\bar{H}}$
M_{ij}	consistent mass matrix
$\vec{n}$	surface normal unit vector
N_g	number of Gauss points in element
N_j	linear shape function
N_n	number of nodes in element
N_r	number of reactions
N_s	number of species
p	pressure
Q	conservative variables or solution vector
R	residual vector
$\bar{\bar{R}}$	right eigenvectors
S	site coefficient
$S^{(\mathrm{v})}$	volume source terms
$\int \mathrm{d}S$	surface integral
t	physical time
T	temperature
$\tilde{T}$	dimensionless temperature
T_c	controlling temperature
T_w	wall temperature
$\vec{u}$	velocity vector
$\bar{v}_{3\mathrm{D},s}$, $\bar{v}_{2\mathrm{D},s}$	mean thermal speeds for volume species and surface species, respectively
$\int \mathrm{d}V$	volume integral
W_i	linear test function

$\vec{x}$	position vector
x_s	species molar fraction
X_s	generic species concentration
y_s	species mass fraction

Greek symbols

β	dimensionless temperature exponent
γ	ratio of mixture heat capacities
γ_s	species recombination efficiency
Γ_s	species impingement flux
ε_{ij}	error estimate
$\vec{\eta}_{ij}, \vec{\chi}_{ij}$	inviscid edge coefficients
κ	mixture thermal conductivity
λ	mixture volume viscosity
λ_s	species loss efficiency
$\bar{\bar{\Lambda}}$	eigenvalues
μ	mixture shear viscosity
ν_{AD}	desorption reaction attempt frequency
ν_r	net stoichiometric exponent for volume species
$\nu'_{r,s}, \nu''_{r,s}$	stoichiometric coefficients for reactant and product side, respectively
ν_ϕ	surface concentration exponent
$\vec{\xi}_i$	nodal boundary coefficient
ρ	mixture density
τ	pseudo time
$\bar{\bar{\tau}}$	shear stress tensor
ϕ	total surface species molar concentration
ϕ_s	surface species molar concentration
$\dot{\omega}_s$	species molar production rate

Nondimensional numbers

Da	Damköhler number
Kn	Knudsen number
Le	Lewis number
Ma	Mach number
Re	Reynolds number
Y^+	dimensionless wall distance

Constants

$N_\mathrm{A} = 6.02214076 \times 10^{23}$	Avogadro constant [1/mol]
$R = 8.31446261815324$	universal gas constant [J/(mol·K)]
$\pi \approx 3.141592653590$	ratio of circumference to diameter of a circle

Subscripts and superscripts

0	standard state value
a	inviscid component
AD	value for adsorption/desorption reaction
b	value for backward reaction
(b)	bulk phase
d	diffusive component
e	element index
ER	value for Eley–Rideal reaction
f	value for forward reaction
g	Gauss point index
i, j	node index
LH	value for Langmuir–Hinshelwood reaction
r	reaction index
ref	reference state value

s	species index
(s)	surface phase
t	thermal component
v	viscous component
(v)	volume phase
w	wall value
∗	discretized value
∞	freestream value

Abbreviations

ACC	advanced carbon-reinforced carbon ablator
AEDC	Arnold Engineering Development Complex
CFD	computational fluid dynamics
CFL	Courant–Friedrichs–Lewy stability condition or Courant number
CIRA	Centro Italiano Ricerche Aerospaziali (Italian Aerospace Research Center)
DLR	Deutsches Zentrum für Luft- und Raumfahrt (German Aerospace Research Center)
DPLR	Data Parallel Line Relaxation Code
FEM	finite element method
FIAT	Fully Implicit Ablation and Thermal Analysis Program
HALO3D	High Altitude Low Orbit 3D Code
ONERA	Office National d'Études et de Recherches Aérospatiales (French Aerospace Research Center)
LAURA	Langley Aerothermodynamic Upwind Relaxation Algorithm
LeMANS	Michigan Aerothermodynamic Navier–Stokes Solver
MOPAR	Modeling of Pyrolysis and Ablation Response Code
NASA	National Aeronautics and Space Administration
PICA	phenolic impregnated carbon ablator
TPS	thermal protection systems

TsNIIMash	Центральный Научно-Исследовательский Институт Машиностроения (Central Research Institute of Machine Building)
US3D	Unstructured 3D Code

Chapter 1. Introduction

1.1. Research motivation

Deployment of civilian satellites into orbit is a fast-expanding market with many privately-owned space companies venturing into the business and competing to make access to space more affordable, reliable, and reusable. The continuous efforts of SpaceX have turned the landing and reusing the first stage of the Falcon 9 orbital rockets from thrilling successes into routine operations. Their demonstrated capability to deploy many satellites in one launch, known as rideshare, together with short turnover times and high launch numbers per rocket boosters, have become decisive advantages that further reduce the costs of orbital deployments. Meanwhile, many other space actors are striving to stretch the limits in different aspects, such as the reusable first stage with electric-pump-fed engines found in Rocket Lab's Electron rockets and the reusable single-stage-to-orbit Skylon spaceplane concept by Reaction Engines Limited with combined-cycle air-breathing engines. Despite the differing strategies, a common denominator is the careful consideration of the atmospheric reentry phase and the integration of reusable thermal protection systems in their designs.

During atmospheric reentry, vehicles experience extreme flow conditions and are subjected to severe mechanical and thermal stresses. The high temperature rise across the strong bow shock appearing around the vehicles promotes the occurrence of complex local thermal and chemical phenomena. In particular, the recombination of dissociated atomic species on the vehicle's surface can significantly alter the gas composition in its vicinity and greatly increase the wall heat flux. The catalytic effects of the surface may be influenced by various factors including gas composition, flow conditions, surface material, surface roughness, and local temperature [1]. Due to their use of low-catalycity materials and coatings to limit surface recombination and reduce heat flux, accurate modeling of gas-surface interactions is paramount in the design of reusable thermal protection systems.

Experimental tests are usually expensive, time consuming, and unable to completely replicate the flow conditions and gas composition. In comparison, numerical simulations, if properly validated, can provide results that are rich in detail, for a wide range of operating conditions and complex geometries. Gas-surface interaction modules have been implemented in various three-dimensional finite volume computational fluid dynamics (CFD) codes and are capable of fast and reliable aerothermal load predictions along the reentry trajectory of hypersonic vehicles, enabling the optimization of designs [2–7].

The High Altitude Low Orbit 3D code (HALO3D) is a comprehensive parallel edge-based finite element all-Mach-number CFD framework for the simulation of flows from subsonic all the way to hypersonic speeds. Past developments have been focusing on the implementation of the Navier–Stokes solver [8], the modeling of chemical reactions that occur in a non-ionized high-temperature environment [9], and the extension to flows deviating from local thermodynamic equilibrium conditions using a two-temperature model and nonequilibrium boundary conditions [10]. A magnetohydrodynamics solver exists to simulate the effect of imposed and/or induced magnetic field for external and internal flows [11, 12], and a direct simulation Monte Carlo solver extends the domain of applicability of HALO3D to the rarefied regime [13].

1.2. High-speed flows

The aerothermal performance of high-speed vehicles can be strongly influenced by the Mach number, Ma, defined as the ratio between the speed of flow and the speed of sound, which is the propagation speed of low-amplitude disturbances within compressible media. As the vehicle approaches and exceeds the speed of sound, the flow behavior around it changes drastically. Using the Mach number as a scaling parameter, four flow regimes can be identified, as shown in Figure 1.1.

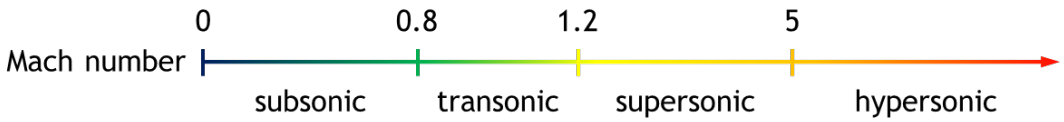

Figure 1.1. Flow regimes.

Above Mach 0.3, the compressibility of the flow becomes non-negligible [14]. In the transonic speeds and above, the wave drag caused by local shock waves becomes significant and the area rule is often employed for drag reduction [15]. At supersonic speeds, the design of the vehicle and propulsion system must take into consideration the significant increase in drag due to shock waves. In the hypersonic regime, of interest in this thesis, aerodynamic heating increases rapidly and becomes the dominant factor in vehicle design [16]. Various flow features distinctive of hypersonic flight as experienced by spacecraft reentering the Earth's atmosphere are shown in Figure 1.2.

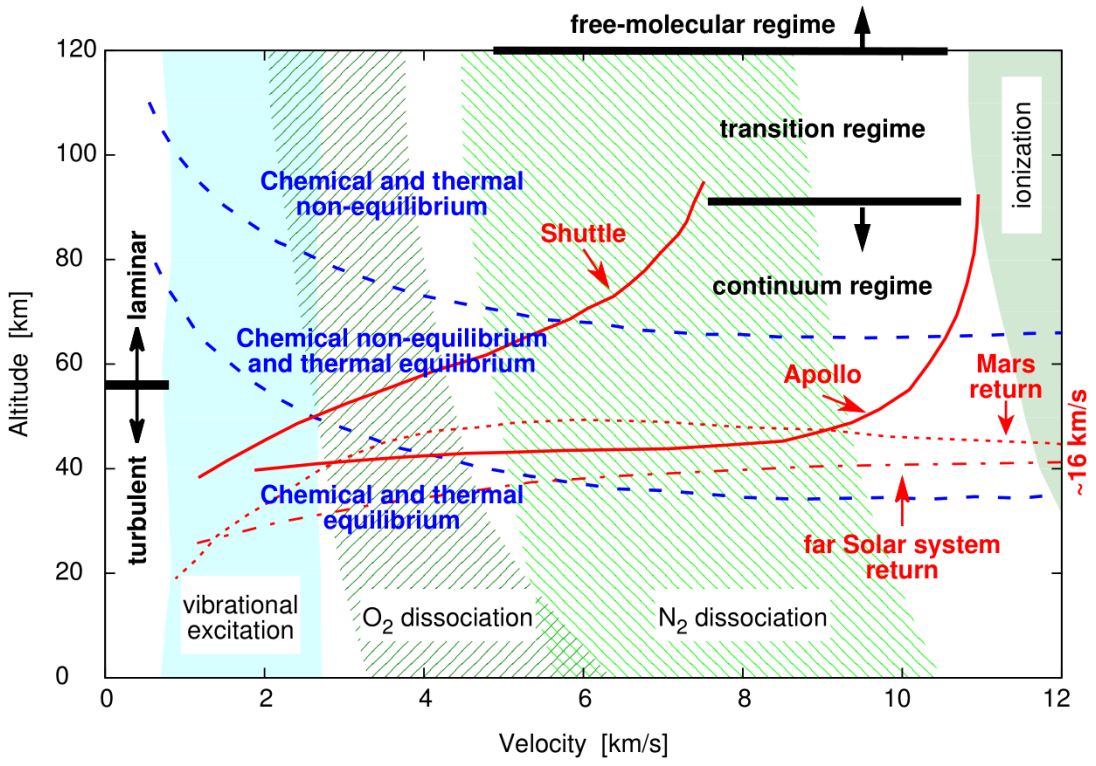

Figure 1.2. Flow features during Earth atmosphere reentry. [17]

As the disturbances created by a supersonic vehicle cannot travel upstream faster than the speed of information propagation, they combine into a shock wave. The flow speed decreases sharply while density, pressure, and temperature increase rapidly in a discontinuous fashion across the shock, with the jumps in the flow field quantities being more pronounced as the Mach number increases. At hypersonic speeds, the temperature after the shock can reach well beyond 10,000 K, exciting the vibrational and electronic energy modes of the molecules and promoting the endothermic dissociation of molecules into atoms. Some of these atoms are then involved in recombination and exchange reactions in the post-shock region. The time scale of these chemical reactions can be compared to the flow time scale through the Damköhler number, Da. When $\mathrm{Da} \ll 1$, the flow passes around the vehicle before reactions can take place and the flow is considered to be chemically frozen. Conversely, when $\mathrm{Da} \gg 1$, the species composition reaches equilibrium very quickly after the shock and the flow is regarded to be in chemical equilibrium. Chemical nonequilibrium conditions, however, occur when the reaction rates share a similar order of magnitude with the convective transport rate ($\mathrm{Da} \approx 1$), leading to spatial variations of the post-shock species composition and requiring detailed modeling of the volume chemistry. Additionally, some of the remaining atomic species are carried through the short shock stand-off distance and may recombine on the surface at different rates, depending on the flow conditions, gas composition, material properties, and local wall temperature. These reactions are exothermic and can significantly increase the wall heat flux. Consequently, detailed analyses of surface catalytic effects are essential for accurate predictions of the aerothermal loads acting on hypersonic vehicles.

At high altitudes where the air density is significantly lower than at sea level, the molecular mean free path, representing the average distance molecules travel between collisions, can be long enough that the continuum assumption breaks down, and the flow medium is better described as a rarefied gas. The Knudsen number, Kn, is an indication of the degree of rarefaction of the flow, defined as the ratio between the molecular mean free path and the characteristic length. At $\mathrm{Kn} \leq 0.01$, the flow is in the continuum regime and is modeled by CFD approaches that solve the Navier–Stokes equations. At $0.01 \leq \mathrm{Kn} \leq 0.1$, the flow is in the continuum-transition regime where CFD techniques are still applicable but slip effects at

the wall must be accounted for. Knudsen number ranges of $0.1 \leq Kn \leq 10$ and $Kn \geq 10$ constitute the transition and free-molecular flow regimes, respectively, in which flow properties are calculated using rarefied gas dynamics solvers such as direct simulation Monte Carlo methods [18, 19].

1.3. Thermal protection systems

Thermal protection systems (TPS) are crucial in protecting the structure and the payload of hypersonic vehicles from heat damage caused by high temperatures on the windward surface. TPS are categorized into two main types: reusable and ablative. Different types of TPS are selected depending on the heat flux, turnaround time, mass, and cost.

Reusable TPS are designed to protect the vehicle over multiple missions without the need for replacement. They are adequate for low reentry speeds along with shallow reentry angles. The reusable TPS used on the Space Shuttle orbiters experienced a peak heat flux of 60 W/cm^2 during their reentries [20]. As shown in part (a) of Figure 1.3, reusable TPS consist of a layer of low catalycity and high emissivity coating and a layer of inorganic low thermal conductivity insulation, both structurally supported by a backup material. Reusable TPS reduce surface heat flux through a three-pronged approach: the low catalycity limits exothermic atomic recombination at the surface, the high emissivity increases the reradiation of energy away from the surface, and the insulation minimizes the conduction of energy into the vehicle.

In comparison, ablative TPS are expended over the course of a single mission. They are suitable for high reentry speeds together with high reentry angles. The Stardust sample return capsule employed an ablative TPS on its forebody to protect against a peak heat flux of 942 W/cm^2 [21]. Ablative TPS are composed mainly of a material that absorbs heat through sublimation and erodes away, with a backup material as support. Depending on the binder used in the ablative material, the TPS can exhibit distinct characteristics. Non-charring ablators are reinforced composites with an inorganic binder. Their main heat

rejection mechanisms are the surface ablation and the mechanical erosion of the inorganic material. Charring ablators are reinforced composites with a polymer resin matrix and their features are illustrated in part (b) of Figure 1.3. The virgin material undergoes pyrolysis which converts carbon into porous char and resin into gases. The gas products carry the energy away and thicken the boundary layer, reducing convective heat transfer to the surface. The porous char also ablates away in a similar fashion as non-charring ablators. Due to the dual heat rejection processes, charring ablators are used for the most severe surface heating conditions.

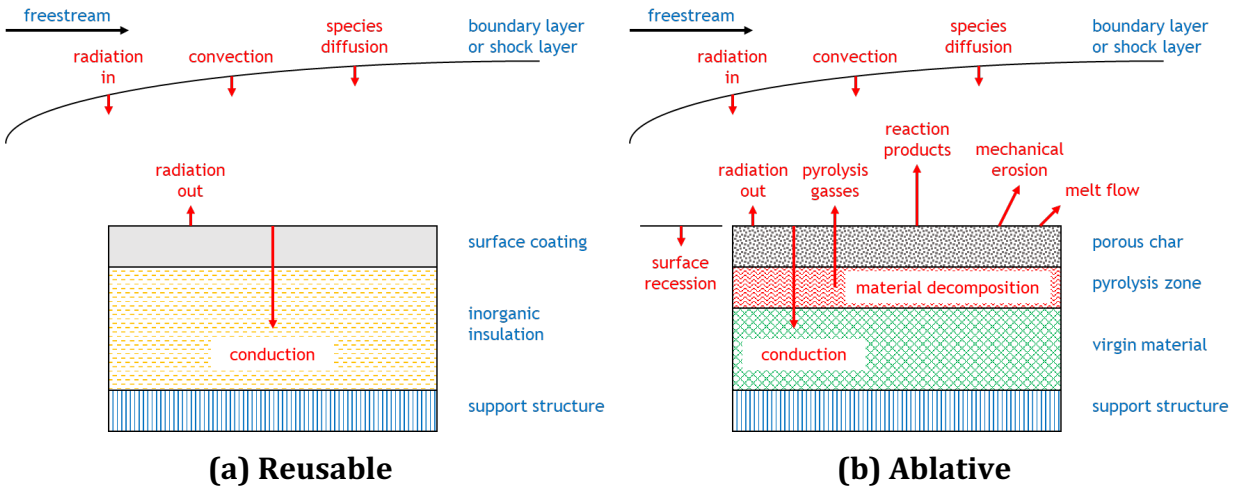

Figure 1.3. Flow features and material composition of reusable and ablative TPS. (adapted from [22])

A selection of current ablative TPS materials and their capabilities are presented in Figure 1.4. The advanced carbon-reinforced carbon ablator (ACC) used on the Genesis probe [23] is of the non-charring type, whereas the Avcoat heatshield (fiberglass honeycomb filled with epoxy resin) used in the Apollo program [24] and the phenolic impregnated carbon ablator (PICA) used in the Stardust [25] and Mars Science Laboratory [26] missions are charring designs. For interplanetary missions, the atmospheric composition and solar radiations impose additional challenges on the TPS designs [27]. Conversely, the Space Shuttle Orbiters employed reusable ceramic tiles consisting of high-temperature reusable surface insulation coated with reaction cured glass [28]. The high emissivity of the coating is achieved by the

black color whereas the low catalycity with respect to N and O is accomplished through the high silica content. The Space Shuttle program demonstrated that with accurate modeling of surface catalycity, reusable TPS designs provide safe and low-cost options for missions with mild reentry conditions.

Forebody heatshield	Flight qualified	Heat flux [W/cm^2]	Pressure [bar]	Entry velocity [km/s]	
				< 13.5	> 13.5
ACC	Genesis	< 800	< 1.0	●	⊘
Avcoat	Apollo	< 1000	< 1.0	●	◒
PICA	Stardust, MSL	< 1800	< 1.5	●	◒
● Fully capable ◒ Potentially capable ⊘ Not capable					

Figure 1.4. Current ablative TPS materials and their capabilities. (adapted from [29])

1.4. Ground test facilities

While flight tests most accurately reproduce the actual conditions, they are prohibitively expensive and can only record a very limited number of parameters, hence ground testing is the preferred experimental method for validating TPS designs. The two main types of existing ground test facilities are arcjet and inductively couple plasma facilities. In an arcjet tunnel, the working gas is heated using electric arcs and accelerated through a converging-diverging nozzle, reproducing hypersonic, high-enthalpy flow. However, the gas is generally limited to air and the atmospheric composition of the outer planets, which predominantly contain H and He, cannot be recreated [27]. Arcjet tunnels may also suffer from contaminated flow due to the erosion of the electrodes. Alternatively, inductively coupled plasma tunnels generate plasma through an induced magnetic field, eliminating flow contamination. Even though only the post-shock subsonic flow conditions are reproduced, the stagnation point heat fluxes encountered in flight can be obtained by matching the in-flight enthalpies, stagnation pressures, and velocity gradients.

Major plasma wind tunnel facilities include NASA Ames and Air Force AEDC in the United States, CIRA in Italy, and TsNIIMash in Russia. The CIRA Scirocco, the world's most powerful plasma wind tunnel, consumes a maximum electrical power of 70 MW at the maximum mass flow rate of 3.5 kg/s using a working gas of air and argon. It can accommodate test articles of up to 2 m in diameter and reproduce a Mach number range from 3 to 12 and a temperature range from 2,000 to 10,000 K [30].

While ground tests are valuable for design validations, they exhibit many deficiencies that impact their accuracy and feasibility. Ground test facilities are capable of limited test conditions per facility, and it can be difficult to simultaneously reproduce the hypersonic speed, enthalpy, gas composition, and model dimension that match the flight conditions. Additionally, only few significant quantities can be measured which limits the ability to visualize complex flow details. Furthermore, the short run times and high operating costs render ground tests expensive timewise and moneywise. Therefore, ground testing is not used to optimize TPS designs, but is instead reserved for developing and selecting TPS materials and validating numerical methods [31].

1.5. Numerical methods

Research into improving the accuracy of numerical methods in modeling gas-surface interactions has been ongoing for several decades. Earlier efforts focused on characterizing the catalycity of dissociated air species through experiments. Goulard presented catalytic efficiencies for N and O from 273 to 673 K on various surface materials and emphasized the superiority of silica compared to metallic surfaces in reducing heat transfer [32]. The analysis of arc plasma data using a nonequilibrium boundary layer code was conducted by Tong to derive effective surface catalycities for N and O recombination [33]. Scott [34] and Kolodziej and Stewart [35] used arc jet stagnation-point heating rates on Space Shuttle ceramic tiles to derive temperature-dependent recombination efficiency curve fits for N and O. The empirically derived recombination efficiencies were used as inputs to the partially

catalytic models coupled with the flow and volume chemistry solvers to estimate surface heat fluxes on reentry bodies [2, 33, 36].

Meanwhile in the chemistry field, theoretical models for surface reactions had been established since the early 1900s. The Langmuir adsorption model involved distinct surface sites and treated binding processes as chemical reactions between adsorbate gas molecules and empty surface sites [37]. The Langmuir–Hinshelwood mechanism, where two atoms adsorb onto neighboring empty surface sites and recombine into one molecule, was suggested by Langmuir in 1922 [38] and further developed by Hinshelwood in 1926 [39]. The Eley–Rideal mechanism, where an atom adsorbs onto an empty surface site and another atom recombines with the first atom directly from the gas phase, was proposed by Eley and Rideal in 1941 [40]. Nonetheless, applications of reaction-based approaches towards gas-surface interactions in hypersonic flows did not commence until the 1990s. Detailed modeling of N and O recombination consisting of the elementary reaction steps was implemented by Deutschmann [41]. The mechanism-based formulation was extended to high-enthalpy CO_2 flows by Thömel, with the reaction rates determined by kinetic Monte Carlo simulations [42]. The finite-rate surface chemistry model established by Marschall and MacLean clarifies implementation details regarding surface and bulk species and allows the representation of both catalytic and ablative reaction types [4, 5]. The ability of the physics-driven approaches to account for competing reactions and surface material properties yields higher-fidelity predictions of near-surface species composition and surface heat fluxes for hypersonic vehicles.

Gas-surface interaction modules have been incorporated into several well-known CFD codes: LAURA from NASA Langley [43], DPLR from NASA Ames [5], LeMANS from the University of Michigan [6], and US3D from the University of Minnesota [7]. Some of the codes have also been coupled with material response modules such as FIAT [44] and MOPAR [45] to model heat conduction and pyrolysis within the surface materials of non-charring and charring ablations.

1.6. Thesis outline and contributions

The present thesis centers on the implementation of physical models and numerical formulations for the simulation of gas-surface interactions. The governing equations and the physical models are introduced in Chapter 2, and the numerical formulations of the edge-based finite element framework are described in Chapter 3. The partially catalytic and finite-rate surface chemistry models are detailed in Chapter 4, and verification and validation test cases for the surface catalycity models are presented in Chapter 5. The conclusion and future developments are listed last in Chapter 6.

The present work aims to increase the capabilities of HALO3D by accounting for gas-surface interactions, which is key in setting accurate mechanical and thermal requirements in the design of TPS. The surface catalycity module containing the partially catalytic and finite-rate surface chemistry models has been implemented as boundary conditions to the flow and volume chemistry solvers. Anisotropic mesh optimization has been incorporated into the solution strategy when using three-dimensional unstructured meshes.

Chapter 2. Physical Modeling

The fluid follows the continuum approximation, where the medium is modeled using continuous functions instead of discrete particles. The viscous compressible Navier–Stokes equations formulated in the Eulerian framework serve as the governing equations. For flows in thermodynamic and chemical equilibrium, the Navier–Stokes equations consist of the conservation of mixture mass, momentum, and energy while body forces are neglected. If the mixture composition varies due to volume or surface reactions, additional equations for the mass conservation of the individual species are included. For all cases presented in this work, thermodynamic equilibrium is assumed, meaning that the translational, rotational, vibrational, and electronic energy modes are described by a single temperature.

2.1. Governing equations

The governing equations in the conservative form can be written as

$$\iiint_V \left[\frac{\partial \vec{Q}}{\partial t} + \nabla \cdot \left(\vec{F}^{\mathrm{a}} - \vec{F}^{\mathrm{v}} - \vec{F}^{\mathrm{d}} - \vec{F}^{\mathrm{t}}\right)\right] \mathrm{d}V = \iiint_V S^{(\mathrm{v})}\, \mathrm{d}V. \tag{2.1}$$

The conservative variables $\vec{Q}$ are expressed as

$$\vec{Q} = \begin{Bmatrix} \rho \\ \rho y_s \\ \rho \vec{u} \\ \rho e \end{Bmatrix}. \tag{2.2}$$

where ρ is the density, y_s is the mass fraction of species s, $\vec{u}$ is the velocity vector, and e is the total energy per unit mass. The inviscid fluxes $\vec{F}^{\mathrm{a}}$ are defined as

$$\vec{F}^{\mathrm{a}} = \begin{Bmatrix} \rho\vec{u} \\ \rho y_s \vec{u} \\ \rho\vec{u} \otimes \vec{u} + \bar{\bar{I}}p \\ (\rho e + p)\vec{u} \end{Bmatrix}, \tag{2.3}$$

where $\otimes$ is the outer product operator, $\bar{\bar{I}}$ is the identity matrix, and p is the pressure. The viscous fluxes $\vec{F}^{\mathrm{v}}$ are given by

$$\vec{F}^{\mathrm{v}} = \begin{Bmatrix} 0 \\ 0 \\ \bar{\bar{\tau}} \\ \bar{\bar{\tau}} \cdot \vec{u} \end{Bmatrix}, \tag{2.4}$$

where the shear stress tensor $\bar{\bar{\tau}}$ can be written as

$$\bar{\bar{\tau}} = \mu[\vec{u} \otimes \nabla + \nabla \otimes \vec{u}] + \lambda(\nabla \cdot \vec{u})\bar{\bar{I}}, \tag{2.5}$$

where μ is the first coefficient of viscosity, i.e., the shear viscosity, and λ is the second coefficient of viscosity, i.e., the volume viscosity. μ and λ are related by the Stokes' hypothesis as $\lambda = -\frac{2}{3}\mu$. The diffusive fluxes $\vec{F}^{\mathrm{d}}$ are expressed as

$$\vec{F}^{\mathrm{d}} = \begin{Bmatrix} 0 \\ \vec{J}_s \\ 0 \\ \sum_{s=1}^{N_s} h_s \vec{J}_s \end{Bmatrix}, \tag{2.6}$$

where N_s is the number of species, $\vec{J}_s$ is the mass flux of species s, and h_s is the specific enthalpy of species s. The thermal fluxes $\vec{F}^{\mathrm{t}}$ are given by

$$\vec{F}^{\mathrm{t}} = \begin{Bmatrix} 0 \\ 0 \\ 0 \\ -\kappa \nabla T \end{Bmatrix}, \tag{2.7}$$

where κ is the mixture's thermal conductivity and T is the temperature. The volume source terms $S^{(\mathrm{v})}$ are defined as

$$S^{(\mathrm{v})} = \begin{Bmatrix} 0 \\ \dot{m}_s^{(\mathrm{v})} \\ 0 \\ 0 \end{Bmatrix}, \tag{2.8}$$

where $\dot{m}_s^{(\mathrm{v})}$ is the volume mass production rate for species s.

2.2. Thermodynamics modeling

The volume medium is assumed to comprise of a mixture of N_s number of ideal gas species. The species and mixture molar concentrations and the molar fractions respect the following relationships

$$c = \sum_{s=1}^{N_s} c_s\,, \qquad x_s = \frac{c_s}{c}, \qquad \sum_{s=1}^{N_s} x_s = 1. \tag{2.9}$$

Similar relationships apply for partial densities and mass fractions

$$\rho = \sum_{s=1}^{N_s} \rho_s\,, \qquad y_s = \frac{\rho_s}{\rho}, \qquad \sum_{s=1}^{N_s} y_s = 1. \tag{2.10}$$

Furthermore, molar concentration and partial density are related by

$$\rho_s = M_s c_s, \qquad \rho = Mc, \tag{2.11}$$

where M_s is the molar mass of species s, while the molar mass of the mixture M is computed as a molar weighted average, as shown below

$$M = \sum_{s=1}^{N_s} x_s M_s. \tag{2.12}$$

Since the species and the mixture follow the ideal gas law, the mixture molar concentration and density can be expressed as

$$c = \frac{p}{RT}, \qquad \rho = \frac{Mp}{RT}, \tag{2.13}$$

where R is the universal gas constant.

The total energy per unit mass in Eq. (2.2) is given by the sum of the kinetic energy and the species internal energies

$$e = \frac{1}{2}(\vec{u} \cdot \vec{u}) + \sum_{s=1}^{N_s} y_s e_s. \tag{2.14}$$

The specific enthalpy is related to the specific energy through

$$h = e + \frac{p}{\rho}. \tag{2.15}$$

For a mixture in thermal equilibrium, the internal energy of species s can be obtained from

$$e_s = c_{\mathrm{v},s} T + e_s^0, \tag{2.16}$$

where e_s^0 is the specific energy of formation which equals to the enthalpy of formation h_s^0 for species s at the reference temperature T_{ref} = 298.15 K. The specific heat capacities at constant volume c_{v} and at constant pressure c_{p} are defined as

$$c_{\text{v}} = \left(\frac{\partial e}{\partial T}\right)_{\text{v}}, \qquad c_{\text{p}} = \left(\frac{\partial h}{\partial T}\right)_{\text{p}}. \tag{2.17}$$

The two specific heat capacities and the ratio of the heat capacities γ are related by

$$c_{\text{p}} - c_{\text{v}} = \frac{R}{M}, \qquad \frac{c_{\text{p}}}{c_{\text{v}}} = \gamma. \tag{2.18}$$

The speed of sound is derived based on classical mechanics [46] from an isentropic process

$$a = \sqrt{\left(\frac{\partial p}{\partial \rho}\right)_{\text{s}}}. \tag{2.19}$$

For a perfect gas, the relationship simplifies to

$$a = \sqrt{\gamma R T} = \sqrt{\gamma \frac{p}{\rho}}. \tag{2.20}$$

For subsonic and low supersonic flows, air can be modeled as calorically perfect, which assumes the specific heat capacities to be constant, and the following relations for species s are valid

$$e_s(T) = c_{\text{v},s} T, \qquad h_s(T) = c_{\text{p},s} T. \tag{2.21}$$

In contrast, for hypersonic flows, air is no longer considered calorically perfect but thermally perfect with specific heat capacities strongly dependent on temperature. The specific energy and the specific enthalpy of species s can be obtained by integrating Eq. (2.17) as

$$\begin{aligned} e_s(T) &= \int_{T_{\mathrm{ref}}}^{T} c_{\mathrm{v},s}(T)\,\mathrm{d}T + h_s^{0,T_{\mathrm{ref}}}, \\ h_s(T) &= \int_{T_{\mathrm{ref}}}^{T} c_{\mathrm{p},s}(T)\,\mathrm{d}T + h_s^{0,T_{\mathrm{ref}}}, \end{aligned} \tag{2.22}$$

where $h_s^{0,T_{\mathrm{ref}}}$ is the enthalpy of formation of species s at the reference temperature.

The integrals for the specific heat capacity at constant pressure, the specific enthalpy, and the specific entropy of gas species were evaluated and published as polynomial fits by NASA [47] as

$$\begin{aligned} \frac{c_{\mathrm{p},s}(T)}{R/M_s} &= a_1T^{-2} + a_2T^{-1} + a_3 + a_4T + a_5T^2 + a_6T^3 + a_7T^4, \\ \frac{h_s^0(T)}{RT/M_s} &= -a_1T^{-2} + a_2\ln(T)\,T^{-1} + a_3 + \frac{1}{2}a_4T + \frac{1}{3}a_5T^2 \\ &\quad + \frac{1}{4}a_6T^3 + \frac{1}{5}a_7T^4 + b_1T^{-1}, \\ \frac{s_s^0(T)}{RT/M_s} &= -\frac{1}{2}a_1T^{-2} - a_2T^{-1} + a_3\ln(T) + a_4T + \frac{1}{2}a_5T^2 \\ &\quad + \frac{1}{3}a_6T^3 + \frac{1}{4}a_7T^4 + b_2. \end{aligned} \tag{2.23}$$

The curve fit coefficients a and b for N, O, N_2, O_2, and NO are organized in Appendix A.1.

2.3. Transport modeling

Mixture viscosity and the thermal conductivity are calculated using Wilke's mixing rule [48] as weighted summations of the corresponding species properties divided by a scaling factor

$$\mu = \sum_{s=1}^{N_s} \frac{x_s \mu_s}{\varphi_s}, \qquad \kappa = \sum_{s=1}^{N_s} \frac{x_s \kappa_s}{\varphi_s}, \tag{2.24}$$

where μ_s and κ_s are the viscosity and the thermal conductivity of species s, respectively, and φ_s is the scaling factor for species s given by

$$\varphi_s = \frac{1}{\sqrt{8}} \sum_{k=1}^{N_s} x_k \frac{\left[1 + \sqrt{\frac{\mu_s}{\mu_k}} \left(\frac{M_k}{M_s}\right)^{\frac{1}{4}}\right]^2}{\sqrt{1 + \frac{M_s}{M_k}}}. \tag{2.25}$$

The viscosities and thermal conductivities of individual species are provided by Blottner and Eucken. Blottner's curve fit for species viscosity is given by [49]

$$\mu_s(T) = 0.1 \exp[(A_s \ln(T) + B_s) \ln(T) + C_s]. \tag{2.26}$$

The curve fit coefficients A_s, B_s, and C_s for N, O, N_2, O_2, and NO are listed in Appendix A.1. The species thermal conductivity for thermal equilibrium can be adapted from Eucken's relation as [50]

$$\kappa_s(T) = \mu_s \left(c_{v,s} + \frac{9}{4} R\right). \tag{2.27}$$

2.4. Diffusion modeling

The diffusion mass flux $\vec{J}_s$ of species s is written according to Fick's law as follows [51]

$$\vec{J}_s = -\rho D_s \nabla y_s, \tag{2.28}$$

where D_s is the diffusion coefficient for species s. The diffusion coefficient is calculated using a Lewis number model that assumes that the effective diffusion coefficient is identical for all neutral species [52], such that

$$D_s = D = \frac{\kappa \mathrm{Le}}{\rho c_\mathrm{p}}, \tag{2.29}$$

with a Lewis number, Le, of 1.4 used in this work. The Lewis number model is appropriate when the species composing the mixture share similar diffusion properties and the flow is non-ionized with the freestream velocity below 8 km/s [53].

2.5. Volume chemistry modeling

Consider a generic reaction r

$$\sum_{s=1}^{N_s} \nu'_{r,s}\, \mathrm{A}_s \underset{k_{\mathrm{b},r}}{\overset{k_{\mathrm{f},r}}{\rightleftharpoons}} \sum_{s=1}^{N_s} \nu''_{r,s}\, \mathrm{A}_s, \tag{2.30}$$

where A_s represents species s, $\nu'_{r,s}$ and $\nu''_{r,s}$ are the stoichiometric coefficients for species s on the reactant and product side, respectively, and $k_{\mathrm{f},r}$ and $k_{\mathrm{b},r}$ are the forward and backward reaction rate coefficients for reaction r, respectively. The volume molar production rate in mol/(m^3·s) for species s due to reaction r is given as

$$\dot{\omega}_{s,r}^{(\mathrm{v})} = \left(\nu_{r,s}'' - \nu_{r,s}'\right)\left(k_{\mathrm{f},r}\prod_{s=1}^{N_s} X_s^{\nu_{r,s}'} - k_{\mathrm{b},r}\prod_{s=1}^{N_s} X_s^{\nu_{r,s}''}\right). \tag{2.31}$$

$\dot{\omega}_s^{(\mathrm{v})}$ due to all volume reactions can be obtained by

$$\dot{\omega}_s^{(\mathrm{v})} = \sum_{r=1}^{N_r} \dot{\omega}_{s,r}^{(\mathrm{v})}, \tag{2.32}$$

and $\dot{m}_s^{(\mathrm{v})}$ can be related to $\dot{\omega}_s^{(\mathrm{v})}$ as follows

$$\dot{m}_s^{(\mathrm{v})} = M_s \dot{\omega}_s^{(\mathrm{v})}. \tag{2.33}$$

For volume reactions, the forward reaction rate coefficient is in the modified Arrhenius form

$$k_{\mathrm{f},r}(T) = C\,\tilde{T}^{\beta}\exp\left(-\frac{T_{\mathrm{c}}}{T}\right), \tag{2.34}$$

where C is the pre-exponential coefficient, $\tilde{T} = T/1\mathrm{K}$ is the dimensionless temperature, and β is the dimensionless temperature exponent, and the controlling temperature $T_{\mathrm{c}} = E_{\mathrm{a}}/R$ is in K. and E_{a} is the activation energy of the reaction. C, β, and T_{c} are specified for a given reaction model. The dimensions of the forward reaction rate coefficients are given by the pre-exponential coefficients.

The backward reaction rate coefficient can be obtained by

$$k_{\mathrm{b},r} = \frac{k_{\mathrm{f},r}}{K_{\mathrm{c},r}}, \tag{2.35}$$

where $K_{\mathrm{c},r}$ is the concentration-based equilibrium constant defined as the ratio between the product side and reactant side species concentrations raised to the stoichiometric coefficients

$$K_{\mathrm{c},r} = \frac{\prod_{s=1}^{N_s} X_s^{\nu''_{r,s}}}{\prod_{s=1}^{N_s} X_s^{\nu'_{r,s}}}. \tag{2.36}$$

Furthermore, $K_{\mathrm{c},r}$ can be related to the activity-based equilibrium constant $K_{\mathrm{a},r}$ by

$$K_{\mathrm{c},r} = K_{\mathrm{a},r} \left(\frac{p_{\mathrm{ref}}}{RT}\right)^{\nu_r}, \tag{2.37}$$

where $p_{\mathrm{ref}} = 10^5$ Pa is the reference pressure [47], and ν_r is the net stoichiometric exponent (product - reactant) for volume species for reaction r. $K_{\mathrm{a},r}$ can be related to the change in Gibbs free energy ΔG_r^0 due to reaction r

$$K_{\mathrm{a},r} = \exp\left(-\frac{\Delta G_r^0(T)}{RT}\right), \tag{2.38}$$

where ΔG_r^0 can be calculated as the stoichiometric-coefficient-weighted summation of the Gibbs free energies G_s^0 of the species involved in reaction r

$$\Delta G_r^0(T) = \left(\sum_{s=1}^{N_s} \nu_s G_s^0(T)\right)_r. \tag{2.39}$$

G_s^0 for volume species s can be derived from the species enthalpy and entropy curve fits from thermodynamic databases [47]

$$G_r^0(T) = h_s^0(T) - T s_s^0(T). \tag{2.40}$$

Chapter 3. Numerical Modeling

3.1. Finite element discretization

Finite element discretization involves dividing the domain into a set of non-overlapping finite elements. The position vector $\vec{x}$ and the dependent variable Q are stored at the nodes belonging to the elements. The values of $\vec{x}$ and Q throughout an element can be approximated through linear combination of the nodal values of the element

$$\begin{aligned} \vec{x}^*(\vec{x},t) &= \sum_{j=1}^{N_n} N_j(\vec{x})\vec{x}_j(t)\,, \\ Q^*(\vec{x},t) &= \sum_{j=1}^{N_n} N_j(\vec{x})Q_j(t), \end{aligned} \tag{3.1}$$

where N_n is the number of nodes in the element, N_j is the piecewise linear shape function of node j of the element, $\vec{x}_j$ and Q_j are the geometry and the dependent variable at node j of the element, respectively, and $\vec{x}^*$ and Q^* are the discretized representations of $\vec{x}$ and Q, respectively. The linear shape function N_j exhibits two basic properties

$$N_j(\vec{x}_i) = \begin{cases} 1 & i = j \\ 0 & i \neq j \end{cases}, \qquad \sum_{j=1}^{N_n} N_j(\vec{x}_i) = 1. \tag{3.2}$$

The weighted residual formulation involves multiplying both sides of the governing equations with the linear test function W_i [54]

$$\sum_{e\in E_i} W_i \iiint_{V_e} \frac{\partial Q}{\partial t}\,\mathrm{d}V + \sum_{e\in E_i} W_i \iiint_{V_e} \nabla\cdot\vec{F}\,\mathrm{d}V = \sum_{e\in E_i} W_i \iiint_{V_e} S^{(\mathrm{v})}\,\mathrm{d}V, \tag{3.3}$$

where E_i is the set of elements sharing node i, and $\vec{F} = \left(\vec{F}^{\mathrm{a}} - \vec{F}^{\mathrm{v}} - \vec{F}^{\mathrm{d}} - \vec{F}^{\mathrm{t}}\right)$ is the combined flux. The integration over V in the governing equations is replaced by a summation over all the elements within the domain V_e. Integrating by parts yields the so-called weak formulation [54]

$$\begin{aligned}&\sum_{e\in E_i}\iiint_{V_e} W_i\frac{\partial Q}{\partial t}\,\mathrm{d}V - \sum_{e\in E_i}\iiint_{V_e}\nabla W_i\cdot\vec{F}\,\mathrm{d}V + \sum_{f\in F_i}\oiint_{S_f} W_i\vec{F}\cdot\vec{n}\,\mathrm{d}S\\&= \sum_{e\in E_i}\iiint_{V_e} W_i S^{(\mathrm{v})}\,\mathrm{d}V,\end{aligned} \tag{3.4}$$

where F_i is the set of faces sharing node i, $\vec{n}$ is the surface normal unit vector. The flux term is divided into the domain contribution and the boundary contribution. Substituting the discretized representation of the variables into the weak formulation yields

$$\begin{aligned}&\sum_{e\in E_i}\sum_{j\in K_e}\iiint_{V_e} W_i N_j\frac{\partial Q_j}{\partial t}\,\mathrm{d}V - \sum_{e\in E_i}\sum_{j\in K_e}\iiint_{V_e} N_j\nabla W_i\cdot\vec{F}_j\,\mathrm{d}V\\&+\sum_{f\in F_i}\sum_{j\in K_e}\oiint_{S_f} W_i N_j\vec{F}_j\cdot\vec{n}\,\mathrm{d}S = \sum_{e\in E_i}\sum_{j\in K_e}\iiint_{V_e} W_i N_j S_j^{(\mathrm{v})}\,\mathrm{d}V,\end{aligned} \tag{3.5}$$

where K_e is the set of nodes belonging to element e. For the Galerkin method, the linear test functions are equal to the linear shape functions, i.e., $W_i = N_i$.

3.2. Edge-based assembly

The classical FEM is formulated in an element-based fashion, which involves integrations using the Gauss–Legendre quadrature, and four levels of loops to assemble the residual vector and the Jacobian matrix [54]. An alternative approach is the edge-based assembly developed by Luo [55], where variables that depend only on geometry are pre-integrated and the residuals and Jacobians are assembled using only two levels of loops, resulting in a significant reduction in computational time and memory requirements. The edge-based

formulation retains the unique applicability of FEM to highly stretched unstructured meshes while allowing for the natural implementation of one-dimensional upwind schemes to improve the stability of the advection terms. In HALO3D, edge-based assembly is employed for residuals in the domain whereas element-based assembly is used for residuals on the boundary.

3.2.1. Mass matrices

The consistent mass matrix M_{ij}, i.e., the edge coefficient, and the lumped mass matrix L_i, i.e., the node contribution, can be introduced

$$\begin{aligned} M_{ij} &= \sum_{e\in E_i} \iiint_{V_e} W_i N_j \,\mathrm{d}V\,, \\ L_i &= \sum_{e\in E_i} \sum_{j\in K_e} \iiint_{V_e} W_i N_j \,\mathrm{d}V = \sum_{e\in E_i} \iiint_{V_e} W_i \,\mathrm{d}V. \end{aligned} \tag{3.6}$$

The mass matrices have two basic properties

$$M_{ij} = M_{ji}, \qquad \sum_{j\in K_e} M_{ij} = L_i. \tag{3.7}$$

The conservative term and the volume source term for node i can be rewritten in an edge-based fashion as

$$\begin{aligned} \sum_{e\in E_i} \sum_{j\in K_e} \iiint_{V_e} W_i N_j \frac{\partial Q_j}{\partial t} \mathrm{d}V &= L_i \frac{\partial Q_i}{\partial t} + \sum_{j\in K_i} M_{ij} \frac{1}{2}\left(\frac{\partial Q_j}{\partial t} - \frac{\partial Q_i}{\partial t}\right), \\ \sum_{e\in E_i} \sum_{j\in K_e} \iiint_{V_e} W_i N_j S_j^{(\mathrm{v})} \,\mathrm{d}V &= L_i S_i^{(\mathrm{v})} + \sum_{j\in K_i} M_{ij} \frac{1}{2}\left(S_j^{(\mathrm{v})} - S_i^{(\mathrm{v})}\right), \end{aligned} \tag{3.8}$$

where K_i is the set of nodes connected to node i via an element edge.

3.2.2. Inviscid fluxes

The edge coefficients $\vec{\eta}_{ij}$ and $\vec{\chi}_{ij}$ can be introduced

$$\begin{aligned}\vec{\eta}_{ij} &= \sum_{e\in E_i} \iiint_{V_e} \left(W_i \nabla N_j - N_j \nabla W_i\right) \mathrm{d}V\,, \\ \vec{\chi}_{ij} &= \sum_{e\in E_i} \oiint_{S_f} W_i N_j \vec{n}\, \mathrm{d}S.\end{aligned} \tag{3.9}$$

Note that $\vec{\chi}_{ij}$ is only defined for boundary edges. The edge coefficients have three basic properties

$$\vec{\eta}_{ii} = 0, \qquad \vec{\eta}_{ij} = -\vec{\eta}_{ji}, \qquad \sum_{j\in K_e} \left(\vec{\eta}_{ij} + \vec{\chi}_{ij}\right) = 0. \tag{3.10}$$

The volume inviscid flux for node i can be rewritten in an edge-based fashion as

$$\begin{aligned}&-\sum_{e\in E_i} \sum_{j\in K_e} \iiint_{V_e} N_j \nabla W_i \cdot \vec{F}_j^{\mathrm{a}}\, \mathrm{d}V \\ &= \sum_{j\in K_i} \vec{\eta}_{ij} \cdot \frac{1}{2}\left(\vec{F}_j^{\mathrm{a}} + \vec{F}_i^{\mathrm{a}}\right) - \sum_{j\in K_i} \vec{\chi}_{ij} \cdot \frac{1}{2}\left(\vec{F}_j^{\mathrm{a}} - \vec{F}_i^{\mathrm{a}}\right).\end{aligned} \tag{3.11}$$

3.2.3. Viscous fluxes

The edge coefficient $\bar{\bar{d}}_{ij}$ is a second order tensor defined as

$$\bar{\bar{d}}_{ij} = \sum_{e\in E_i} \iiint_{V_e} \nabla W_i \cdot \nabla N_j\, \mathrm{d}V, \tag{3.12}$$

$\bar{\bar{d}}_{ij}$ can be rewritten as the symmetric part $\bar{\bar{d}}_{ij}^{\mathrm{s}}$ and the anti-symmetric part $\bar{\bar{d}}_{ij}^{\mathrm{a}}$

$$\bar{\bar{d}}_{ij}^{\mathrm{s}} = \frac{1}{2}\left[\bar{\bar{d}}_{ij} + \left(\bar{\bar{d}}_{ij}\right)^{\mathrm{T}}\right], \qquad \bar{\bar{d}}_{ij}^{\mathrm{a}} = \frac{1}{2}\left[\bar{\bar{d}}_{ij} - \left(\bar{\bar{d}}_{ij}\right)^{\mathrm{T}}\right]. \tag{3.13}$$

The assembly of the stress tensor for node i can be rewritten in an edge-based fashion as

$$\begin{aligned} &\sum_{e\in E_i}\sum_{j\in K_e}\iiint_{V_e} N_j \nabla W_i \cdot \bar{\bar{\tau}}\,\mathrm{d}V \\ &= \sum_{j\in K_i}\left\{\left[\mu_{ij}\mathrm{tr}\left(\bar{\bar{d}}_{ij}\right)\bar{\bar{I}} + \left(\lambda_{ij}+\mu_{ij}\right)\bar{\bar{d}}_{ij}^{\mathrm{s}} + \left(\lambda_{ij}-\mu_{ij}\right)\bar{\bar{d}}_{ij}^{\mathrm{a}}\right]\left(\vec{u}_j - \vec{u}_i\right)\right\}, \end{aligned} \tag{3.14}$$

where tr() is the trace operator. Similarly, the assembly of the inner product of the stress tensor and velocity for node i can be rewritten in an edge-based fashion as

$$\begin{aligned} &\sum_{e\in E_i}\sum_{j\in K_e}\iiint_{V_e} N_j \nabla W_i \cdot \left(\bar{\bar{\tau}}\cdot\vec{u}\right)\mathrm{d}V \\ &= \sum_{j\in K_i}\left\{\left[\mu_{ij}\mathrm{tr}\left(\bar{\bar{d}}_{ij}\right)\bar{\bar{I}} + \left(\lambda_{ij}+\mu_{ij}\right)\bar{\bar{d}}_{ij}^{\mathrm{s}} + \left(\lambda_{ij}-\mu_{ij}\right)\bar{\bar{d}}_{ij}^{\mathrm{a}}\right]:\vec{u}_{ij}\left(\vec{u}_j - \vec{u}_i\right)\right\}, \end{aligned} \tag{3.15}$$

where the column product between two second-order tensors is defined as

$$\bar{\bar{A}}:\bar{\bar{B}} = \sum_i\sum_j A_{ij}B_{ij}, \tag{3.16}$$

where A_{ij} and B_{ij} are components of $\bar{\bar{A}}$ and $\bar{\bar{B}}$, respectively.

3.3. Roe's scheme

The average of inviscid fluxes at nodes i and j are estimated by solving the approximate Riemann problem between the two nodes. The Roe scheme is used in the flow solver [56], as shown below

$$\begin{aligned}&\left\{\vec{\eta}_{ij}\frac{1}{2}\left[\vec{F}^{\mathrm{a}}(Q_i)+\vec{F}^{\mathrm{a}}\left(Q_j\right)\right]\right\}_{\mathrm{Roe}}\\&=\vec{\eta}_{\mathrm{LR}}\frac{1}{2}\left[\vec{F}^{\mathrm{a}}(Q_{\mathrm{L}})+\vec{F}^{\mathrm{a}}(Q_{\mathrm{L}})\right]-\frac{1}{2}\left|\tilde{A}\left(Q_{\mathrm{L}},Q_{\mathrm{R}},\vec{\eta}_{ij}\right)\right|(Q_{\mathrm{L}}-Q_{\mathrm{R}}),\end{aligned} \tag{3.17}$$

where Q_{L} and Q_{R} denote the left state and right state of the Riemann problem, respectively, and the Roe matrix $\tilde{A}$ satisfy the following properties:

1. $\tilde{A}$ is diagonalizable with real eigenvalues,
2. $\tilde{A}(Q_{\mathrm{L}},Q_{\mathrm{R}})\to A$ as $Q_{\mathrm{L}}\to 0$ and $Q_{\mathrm{R}}\to 0$,
3. $\tilde{A}(Q_{\mathrm{L}},Q_{\mathrm{R}})\cdot(Q_{\mathrm{L}}-Q_{\mathrm{R}})=\vec{F}^{\mathrm{a}}(Q_{\mathrm{R}})-\vec{F}^{\mathrm{a}}(Q_{\mathrm{L}})$.

The Roe average state is defined as

$$\begin{aligned}\tilde{\rho}&=\sqrt{\rho_{\mathrm{L}}\rho_{\mathrm{R}}},\\\tilde{\vec{u}}&=\frac{\sqrt{\rho_{\mathrm{L}}}\vec{u}_{\mathrm{L}}+\sqrt{\rho_{\mathrm{R}}}\vec{u}_{\mathrm{R}}}{\sqrt{\rho_{\mathrm{L}}}+\sqrt{\rho_{\mathrm{R}}}},\\\tilde{h}&=\frac{\sqrt{\rho_{\mathrm{L}}}h_{\mathrm{L}}+\sqrt{\rho_{\mathrm{R}}}h_{\mathrm{R}}}{\sqrt{\rho_{\mathrm{L}}}+\sqrt{\rho_{\mathrm{R}}}},\\\tilde{a}&=\sqrt{(\gamma-1)\left(\tilde{h}-\frac{1}{2}\tilde{\vec{u}}\cdot\tilde{\vec{u}}\right)}.\end{aligned} \tag{3.18}$$

The Roe matrix $\tilde{A}$ can be decomposed as

$$\tilde{A}=\tilde{L}\tilde{\Lambda}\tilde{R}, \tag{3.19}$$

where the eigenvalue matrix $\widetilde{\Lambda}$ can be expressed using the Roe average state as

$$\widetilde{\Lambda} = [\tilde{u}_n - \tilde{a}, \tilde{u}_n, \tilde{u}_n, \tilde{u}_n, \tilde{u}_n + \tilde{a}]\bar{\bar{I}}_{5\times5}, \tag{3.20}$$

where $\tilde{u}_n$ is the Roe average velocity projected along $\vec{\eta}_{\mathrm{LR}}$, as shown below

$$\tilde{u}_n = \tilde{u} \cdot \frac{\vec{\eta}_{\mathrm{LR}}}{|\vec{\eta}_{\mathrm{LR}}|}. \tag{3.21}$$

3.4. Boundary conditions

The boundary terms in the governing equations are treated differently for inviscid and viscous flows.

3.4.1. Inviscid flow

The inviscid boundary terms in the governing equations can be reformulated as

$$\sum_{f\in F_i}\sum_{j\in K_e}\oiint_{S_f} W_i N_j \vec{F}_j^{\mathrm{a}} \cdot \vec{n}\,\mathrm{d}S = \sum_{f\in F_i}\oiint_{S_f} W_i \vec{F}^{\mathrm{a}}\left(\sum_{j\in K_i} N_j Q_j\right)\cdot \vec{n}\,\mathrm{d}S. \tag{3.22}$$

The fluxes are rewritten in a node-based form

$$\sum_{f\in F_i}\sum_{j\in K_e}\oiint_{S_f} W_i N_j \vec{F}_j^{\mathrm{a}} \cdot \vec{n}\,\mathrm{d}S = \vec{\xi}_i \cdot \vec{F}^{\mathrm{a}}(Q_i) + \sum_{j\in K_i} \vec{\chi}_{ij}\left[\vec{F}^{\mathrm{a}}(Q_j) - \vec{F}^{\mathrm{a}}(Q_i)\right], \tag{3.23}$$

where the nodal boundary coefficient $\vec{\xi}_i$ is defined as

$$\vec{\xi}_i = \sum_{f \in F_i} \oiint_{S_f} W_i \vec{n} \, \mathrm{d}S. \tag{3.24}$$

3.4.2. Viscous flow

The inviscid fluxes are assembled in an element-based fashion

$$\sum_{f \in F_i} \sum_{j \in K_e} \oiint_{S_f} W_i N_j \vec{F}_j^{\mathrm{a}} \cdot \vec{n} \, \mathrm{d}S = \sum_{f \in F_i} \sum_{g=1}^{N_g} \left[w_g W_i(\vec{x}_g) \vec{F}^{\mathrm{a}} \left(Q(\vec{x}_g) \right) \cdot \vec{n}(\vec{x}_g) \right]. \tag{3.25}$$

The viscous fluxes are also assembled in an element-based fashion

$$\sum_{f \in F_i} \sum_{j \in K_e} \oiint_{S_f} W_i N_j \vec{F}_j^{\mathrm{v}} \cdot \vec{n} \, \mathrm{d}S = \sum_{f \in F_i} \sum_{g=1}^{N_g} \left[w_g W_i(\vec{x}_g) \vec{F}^{\mathrm{v}} \left(Q(\vec{x}_g) \right) \cdot \vec{n}(\vec{x}_g) \right]. \tag{3.26}$$

3.4.3. Supersonic inlets and outlets

In a supersonic flow, all flow properties are influenced solely by upstream conditions. Therefore, at the supersonic inlet, the values of all conservative variables must be specified, whereas, at the supersonic outlet, the values of all conservative variables have already been determined.

3.4.4. Slip wall

The slip wall boundary condition is given as

$$\sum_{f \in F_i} \sum_{j \in K_e} \oiint_{S_f} W_i N_j \vec{F}_j^{\mathrm{a,w}} \cdot \vec{n} \, \mathrm{d}S = \left[0, \vec{\xi}_i p_i, 0 \right]. \tag{3.27}$$

The inviscid surface fluxes for the species mass and energy conservation equations vanish since the velocity component normal to the wall is zero, as shown by

$$(\rho y_s \vec{u}) \cdot \vec{n} = 0, \qquad (\rho e + p)\vec{u} \cdot \vec{n} = 0. \tag{3.28}$$

3.4.5. Dirichlet boundary conditions

Dirichlet boundary conditions for primitive variables such as velocity, species mass fractions, and temperatures are often prescribed at the walls. Since the governing equations are defined in terms of conservative variables, the constraints on the primitive variables must be expressed in terms of conservative variables.

The no-slip wall boundary condition assumes that a viscous fluid in direct contact with a solid boundary has zero velocity relative to the boundary. The zero-velocity condition can be enforced by imposing a zero value and a zero change for momentum, a conservative variable, at the wall

$$\rho\vec{u} = 0, \qquad \Delta(\rho\vec{u}) = 0. \tag{3.29}$$

Imposing fixed species mass fractions at the wall is equivalent to specifying $\Delta y_s = 0$ in the species mass conservation equations, which gives

$$(1 - y_s)\Delta(\rho y_s) - y_s \sum_{i=1, i\neq s}^{N_s} \Delta(\rho y_s) = 0. \tag{3.30}$$

The fixed temperature boundary condition can be enforced by setting $\Delta T = 0$ in the energy conservation equation, which yields

$$\left(\frac{1}{2}\vec{u} \cdot \vec{u} - e_{\text{int}}\right)\Delta\rho - \vec{u} \cdot \Delta(\rho\vec{u}) + \Delta e = 0, \tag{3.31}$$

where e_{int} is the internal energy per unit mass.

3.5. Temporal discretization

Assuming a governing equation with a conservative variable Q

$$K\frac{\partial Q}{\partial t} = R(Q), \tag{3.32}$$

where Q is the solution vector, K is the mass matrix, and R is the residual vector.

3.5.1. Steady-state simulations

For steady-state simulations, a Newton-Raphson procedure is used in a fully implicit manner

$$Q^n - Q^{n-1} = A^{-1}(Q^n)R(Q^n), \tag{3.33}$$

where the Jacobian matrix A with the contribution of the pseudo timestep is given as

$$A(Q^n) = \frac{K}{\Delta\tau^n}\bar{\bar{I}} + \left(\frac{\partial R}{\partial Q}\right)_n. \tag{3.34}$$

The pseudo timestep $\Delta\tau^n$ is determined by locally satisfying the Courant–Friedrichs–Lewy (CFL) stability condition [57], given as

$$\text{CFL} = \frac{u_{\max}\Delta\tau^n}{\Delta x}, \tag{3.35}$$

where CFL is the Courant number, $u_{\max}$ is the maximum wave speed at the current node, and Δx is the element edge length.

3.5.2. Transient simulations

For transient simulations, the solution is computed in a fully explicit manner

$$Q^n - Q^{n-1} = \frac{2}{3}\Delta t K^{-1} R(Q^{n-1}) + \frac{1}{3}(Q^{n-1} - Q^{n-2}), \tag{3.36}$$

where the physical time derivative term is discretized in the second order Gear's scheme [58]

$$\frac{\partial Q^n}{\partial t} = \frac{1}{\Delta t}\left(\frac{3}{2}Q^n - 2Q^{n-1} + \frac{1}{2}Q^{n-2}\right). \tag{3.37}$$

3.6. Anisotropic mesh optimization

For CFD simulations, it is paramount that the meshes are well aligned with singular phenomena of fluid dynamics, such as shocks, boundary layers, and shear layers. Misaligned grids can result in poor resolutions of the phenomena and significant reductions in the solution accuracy. For simulations with complex geometries, it is nearly impossible to generate meshes that are well aligned with the singular phenomena when their occurrences and locations are unknown a priori. To overcome this limitation, an automatic anisotropic mesh optimization code, OptiGrid, developed by the McGill CFD Laboratory [59], that couples solver and mesh during iterations, is used to directionally refine the mesh for the unstructured grid simulations presented in this work.

The singular phenomena cited above are almost unidirectional, where the gradients are much higher in one principal direction than in the other two. Mesh enrichment techniques based solely on gradients are unable to identify the direction with highest gradient, leading to excessive refinement in the directions of lower gradients. The resulting grids are large but remain poorly optimized with respect to global metrics, rendering gradient-based approaches impractical for 3D applications. Therefore, the goal of the OptiGrid algorithm is

to intelligently introduce the directionality required to produce a well-aligned grid without necessarily increasing the number of elements or nodes.

The anisotropic adaptation is achieved through the equi-distribution of the truncation error, defined as the difference between the partial differential equation and its discretized form. While the exact solution is unknown, the error can be estimated using the Hessian matrix $\bar{\bar{H}}$ of a few solution scalar variables chosen based on the nature of the problem being solved,

$$\bar{\bar{H}} = \bar{\bar{R}}\bar{\bar{\Lambda}}\bar{\bar{R}}^{\mathrm{T}}, \tag{3.38}$$

where $\bar{\bar{\Lambda}}$ and $\bar{\bar{R}}$ are the eigenvalues and the right eigenvectors of the variables, respectively. A metric $\bar{\bar{M}}$ based on $\bar{\bar{H}}$ is created to avoid issues with negative eigenvalues.

$$\bar{\bar{M}} = \bar{\bar{R}}\left|\bar{\bar{\Lambda}}\right|\bar{\bar{R}}^{\mathrm{T}}. \tag{3.39}$$

The error estimate ε_{ij} is defined based on $\bar{\bar{M}}$ in an edge-based fashion as,

$$\varepsilon_{ij} = \int_0^1 \sqrt{\left(\vec{x}_i - \vec{x}_j\right)^{\mathrm{T}} \bar{\bar{M}}(l) \left(\vec{x}_i - \vec{x}_j\right)}\, \mathrm{d}L, \tag{3.40}$$

where $\vec{x}_i$ and $\vec{x}_j$ are two endpoints of an edge.

The error estimate can be considered as a transformation of the mesh where edgewise errors in physical space are represented as edge lengths in the metric space. Thus, the objective of the optimizer is to obtain equal edge lengths in the metric space, which is synonym to equi-distributing the error estimate in the physical space. The optimization process involves multiple solution-adaptation cycles specified by the user. First, an initial solution is obtained from the flow solver using the original grid. Then, OptiGrid calculates the error estimate based on the gird and the solution and modifies the grid. Within each adaptation cycle, a combination of four basic mesh operations: refinement, coarsening, node movement, and

edge swapping are performed while preserving the physical geometry of 3D object being analyzed. Each adaptation cycle is controlled by an optimization target, defined to be either a prescribed error level in the solution or a certain number of nodes or elements. The latter option is used in this work to limit mesh sizes. After the mesh modifications, the solution obtained using the old grid is interpolated onto the new grid, to serve as the restart solution for the next cycle.

With OptiGrid, solutions of better accuracies can be obtained using drastically fewer nodes on unstructured meshes [60]. Consequently, when using unstructured meshes for hypersonic vehicles with complex geometries, anisotropic mesh optimization is indispensable for achieving accurate aerothermal predictions.

Chapter 4. Gas-Surface Interactions

4.1. Surface catalycity

Surface catalycity is commonly described by the following five approaches, three of which are illustrated in Figure 4.1:

- The **noncatalytic model** supposes that none of the impinging atoms on the surface are recombining. This model provides the theoretical lower limit for the heat flux.
- The **supercatalytic model** dictates that the species mass fractions on the surface match the free-stream gas composition.
- The **partially catalytic model** assumes that a given fraction of the impinging atoms recombines on the surface. This recombination efficiency, denoted by γ, may be taken as a constant or be temperature dependent.
- The **fully catalytic model** assumes that all impinging atoms recombine on the surface and is therefore equivalent to the partially catalytic model with $\gamma = 1$. This model provides the theoretical upper limit for the wall heat flux.
- The **finite-rate surface chemistry model** accounts for detailed surface chemical reactions and surface material properties to update the species composition on the surface.

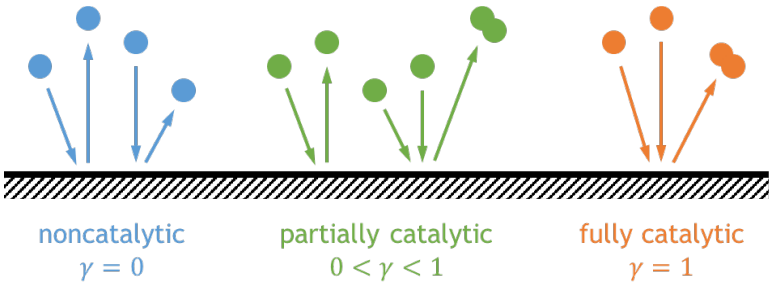

Figure 4.1. Surface catalycity models.

4.2. Species mass conservation at the surface

For a steady-state compressible viscous gas mixture on a no-slip, no-penetration, catalytic surface, the diffusion mass flux of species s to the wall must be balanced by the mass production rate of species s at the wall [7]

$$\oiint_S \vec{J}_s \cdot \vec{n}\, \mathrm{d}S = \oiint_S \dot{m}_s^{(\mathrm{s})}\, \mathrm{d}S, \tag{4.1}$$

where $\dot{m}_s^{(\mathrm{s})}$ is the surface mass production rate for species s. Simplifying yields the species mass conservation on the surface

$$\vec{J}_s \cdot \vec{n} = \dot{m}_s^{(\mathrm{s})}. \tag{4.2}$$

4.3. Energy conservation at the surface

For a steady-state compressible viscous gas mixture on a no-slip, no-penetration, catalytic surface, in the absence of volumetric energy sources, energy dissipation due to the surface shear stress, and energy transfer due to radiation, the energy conservation simplifies to the thermal fluxes and the diffusive fluxes [6]

$$\oiint_S \left(-\kappa \nabla T + \sum_{s=1}^{N_s} h_s \vec{J}_s \right) \cdot \vec{n}\, \mathrm{d}S = 0. \tag{4.3}$$

Rearranging and substituting the species diffusion mass fluxes with the species mass production rates yields

$$-\kappa \nabla T \cdot \vec{n} = -\sum_{s=1}^{N_S} h_s \vec{J}_s \cdot \vec{n} = -\sum_{s=1}^{N_S} h_s \dot{m}_s^{(\mathrm{s})} . \tag{4.4}$$

4.4. Surface thermodynamic properties

The mean thermal speeds on the surface are defined differently for species of different phases. For a volume species s, $\bar{v}_{3\mathrm{D},s}$ is given by

$$\bar{v}_{3\mathrm{D},s} = \sqrt{\frac{8RT_{\mathrm{w}}}{\pi M_s}}, \tag{4.5}$$

and for a surface species s, $\bar{v}_{2\mathrm{D},s}$ is given by

$$\bar{v}_{2\mathrm{D},s} = \sqrt{\frac{\pi RT_{\mathrm{w}}}{2M_s}}. \tag{4.6}$$

where T_{w} is the wall temperature. The impingement flux Γ_s for a volume species s is defined as the molar flux towards the surface phase due to collisions with the surface, and can be calculated from the mean thermal speed using kinetic theory [61] as

$$\Gamma_s = c_s \frac{\bar{v}_{3\mathrm{D},s}}{4} = c_s \sqrt{\frac{RT_{\mathrm{w}}}{2\pi M_s}}. \tag{4.7}$$

4.5. Partially catalytic model

To model the recombination of atomic species s on the surface, the partially catalytic model assumes a recombination efficiency defined as

$$\gamma_s = \frac{-\dot{\omega}_s^{(\mathrm{s})}}{\Gamma_s}, \tag{4.8}$$

where γ_s is the recombination efficiency of species s, and $-\dot{\omega}_s^{(\mathrm{s})}$ is the molar flux due to the recombination of species s, i.e., the consumption rate of species s. The negative sign is to convert from the consumption rate to the production rate. The surface molar production rate of species s can be calculated as

$$\dot{\omega}_s^{(\mathrm{s})} = -\gamma_s \Gamma_s = -\gamma_s c_s \sqrt{\frac{RT_{\mathrm{w}}}{2\pi M_s}}, \tag{4.9}$$

and the surface mass production rate of species s can be calculated as

$$\dot{m}_s^{(\mathrm{s})} = M_s \dot{\omega}_s^{(\mathrm{s})} = -\gamma_s M_s c_s \sqrt{\frac{RT_{\mathrm{w}}}{2\pi M_s}} = -\gamma_s \rho y_s \sqrt{\frac{RT_{\mathrm{w}}}{2\pi M_s}}, \tag{4.10}$$

where ρ is the mixture density, and y_s is the mass fraction of species s. The negative sign is to convert from the recombination flux which is the consumption rate to the production rate.

The recombination efficiency is a macroscopic description of surface catalycity that represents the overall conversion efficiency between a given pair of atomic and molecular species. The efficiency is not based on individual chemical reaction rates but is instead derived from empirical results under specific conditions: temperature, pressure, gas composition, and surface material properties.

The recombination efficiency model limits each pair of atomic and molecular species to be uniquely associated with each other. Thus, the model does not account for competing mechanisms where one atomic species can recombine into different molecular species, or vice versa. The standard procedure is to neglect secondary pairings of atomic and molecular species, such as the recombination of N and O to form NO for the five-species model (N, O, N_2, O_2, NO), yielding the recombination efficiency as $\vec{\gamma} = \{-\gamma_N, -\gamma_O, \gamma_N, \gamma_O, 0\}^T$ [33, 36].

The recombination efficiency can be given as constant or temperature dependent. The constant recombination efficiency model is sufficient for simulations where the surface temperature is fixed or barely varying over a body. It is a common approach by several authors to use constant values of γ and to assume the same efficiency for N and O, $\gamma_N = \gamma_O$, for the five-species model (N, O, N_2, O_2, NO) [2].

On the other hand, experimental results indicate a temperature dependency for the recombination efficiency, as γ can increase several folds in just a few hundred kelvins. This variation can be adequately described by an exponential fit, as shown by the coefficients for species N and O reported below in Equations (4.11) [34] and (4.12) [35]. The values of the recombination efficiencies from 950 K to 1900 K are plotted in Figure 4.2. Since recombination efficiencies depend solely on the wall temperature, using temperature-dependent γ values with an isothermal wall boundary condition is equivalent to setting γ values to be constant across the entire catalytic surface.

$$\text{Scott}\begin{cases}\gamma_{\mathrm{N}} = 7.14\times10^{-2}\times\exp\left(-\dfrac{2219}{T_{\mathrm{w}}}\right), & 950\ \mathrm{K} < T_{\mathrm{w}} < 1670\ \mathrm{K}\\ \gamma_{\mathrm{O}} = 1.6\times10^{+1}\times\exp\left(-\dfrac{10271}{T_{\mathrm{w}}}\right), & 1400\ \mathrm{K} < T_{\mathrm{w}} < 1650\ \mathrm{K}\end{cases} \tag{4.11}$$

$$\text{Kolodziej}\begin{cases}\gamma_{\mathrm{N}} = 6.1\times10^{-2}\times\exp\left(-\dfrac{2480}{T_{\mathrm{w}}}\right), & 1410\ \mathrm{K} < T_{\mathrm{w}} < 1640\ \mathrm{K}\\ \gamma_{\mathrm{N}} = 6.1\times10^{-4}\times\exp\left(+\dfrac{5090}{T_{\mathrm{w}}}\right), & 1640\ \mathrm{K} < T_{\mathrm{w}} < 1905\ \mathrm{K}\\ \gamma_{\mathrm{O}} = 4.0\times10^{+1}\times\exp\left(-\dfrac{11440}{T_{\mathrm{w}}}\right), & 1435\ \mathrm{K} < T_{\mathrm{w}} < 1580\ \mathrm{K}\\ \gamma_{\mathrm{O}} = 3.9\times10^{-8}\times\exp\left(+\dfrac{21410}{T_{\mathrm{w}}}\right), & 1580\ \mathrm{K} < T_{\mathrm{w}} < 1845\ \mathrm{K}\end{cases} \tag{4.12}$$

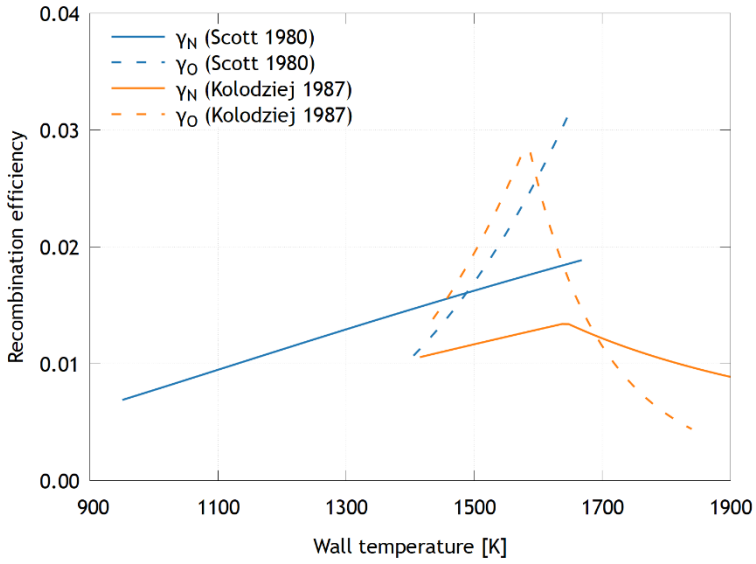

Figure 4.2. Recombination efficiencies of N and O vs. temperature.

4.6. Finite-rate surface chemistry model

The finite-rate surface chemistry model is the next step towards more accurate simulations of gas-surface interactions by employing detailed surface reaction mechanisms and taking into consideration surface material properties for a microscopic and physically justified approach. Finite-rate surface chemistry attempts to recreate heterogeneous reactions using modified procedures based on those used for homogeneous volume reactions. Central to the description are pseudo species on the surface that not only provide locations and pathways for the multiphase interactions to occur but also enable competing surface reaction mechanisms.

4.6.1. Species phases modeling

Volume, surface, and bulk environments can coexist at the gas-surface interface. Physically distinct regions within each environment are represented by one or more phases. In this work, each environment can be sufficiently described with only one phase.

Finite-rate surface chemistry requires a distinct treatment for species in different phases. The volume phase includes all species that originate from the freestream as well as species that are released from the bulk environment into the volume through the consumption of surface material. In the following, the symbol for a volume species is not followed by anything.

The surface phase contains one or more sets of active sites on which all surface reactions must take place. Each set of active sites has finite surface molar concentrations and may be only active for a certain set of mechanisms, which together reflect the catalytic ability of the surface material toward different reactions. Each active site may be vacant or may contain a single adsorbed atom or molecule. All surface reactions must involve at least one surface species on each side but not more than one set of active sites across both sides. The symbol for a surface species is followed by “(s)”, including empty surface sites denoted as “E(s)”, and

adsorption atomic and molecular species, e.g., “N(s)” and “O(s)”. Partial densities and mass fractions for surface species are undefined due to empty surface sites having zero mass. Thus, surface species quantities must be expressed in terms of molar concentrations and molar fractions.

The bulk phase represents species that constitute the surface material. Bulk species enable the modeling of the transfer of material from bulk toward the volume through ablation, as well as the surface dependency on sublimation/deposition reaction. The symbol for a bulk species is followed by “(b)”.

The concentrations of the species X_s have different definitions and units depending on the phase. For a volume species A, X_{A} represents the volume molar concentration with units of mol/m^3: $X_{\mathrm{A}} = c_{\mathrm{A}}$. For a surface species A(s), $X_{\mathrm{A(s)}}$ denotes the surface molar concentration with units of mol/m^2: $X_{\mathrm{A(s)}} = \phi_{\mathrm{A(s)}}$. For a bulk species A(b), $X_{\mathrm{A(b)}}$ equals the bulk molar fraction and is nondimensional: $X_{\mathrm{A(b)}} = x_{\mathrm{A(b)}}$.

The surface coverage for a surface species A(s) is defined as the ratio of the molar concentration of the surface species over the total molar concentration of all surface species, akin to the molar fraction for volume species

$$x_{\mathrm{A(s)}} = \frac{\phi_{\mathrm{A(s)}}}{\phi}. \tag{4.13}$$

4.6.2. Surface reactions modeling

Surface production rates $\dot{\omega}_{s,r}^{(\mathrm{s})}$, $\dot{\omega}_{s}^{(\mathrm{s})}$, and $\dot{m}_{s}^{(\mathrm{s})}$ are calculated in the identical fashion as their volume counterparts using Equations (2.31), (2.32), and (2.33), respectively. Unlike volume reactions, the dimensions of the species concentrations in the surface formulation can vary depending on the phase, and the surface production rates are expressed per unit area instead of per unit volume.

The three surface reaction types considered in this thesis are described below and illustrated in Figure 5.12:

- Adsorption/Desorption (AD): $A + E(s) \rightleftharpoons A(s)$
- Eley–Rideal (ER): $A + B(s) \rightleftharpoons AB + E(s)$
- Langmuir–Hinshelwood (LH): $A(s) + B(s) \rightleftharpoons AB + 2E(s)$

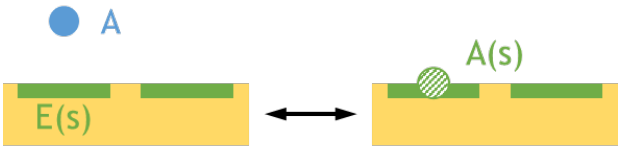

(a) Adsorption/Desorption

(b) Eley–Rideal

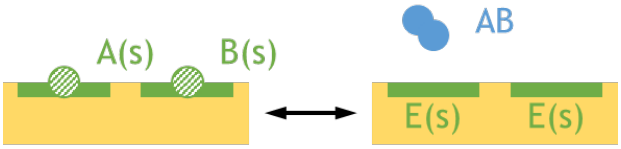

(c) Langmuir–Hinshelwood

Figure 4.3. Surface reaction types.

4.6.3. Forward reaction rate coefficients

For surface reactions, the forward reaction rate coefficient is in the modified Arrhenius form

$$k_{f,r}(T_w) = S\ C\ \tilde{T}_w^{\beta} \exp\left(-\frac{T_c}{T_w}\right), \tag{4.14}$$

where S is the site coefficient, and $\tilde{T}_\mathrm{w} = T_\mathrm{w}/1\mathrm{K}$ is the dimensionless wall temperature. C, β, and T_c are specified for a given reaction model. For surface reactions, the pre-exponential coefficients are dimensionless, and the dimensions of the forward reaction rate coefficients are given by the site coefficients. S differs in form for the different surface reaction types as shown in Table 4.1.

Table 4.1. Site coefficient for surface reaction types.

Type	Site Coefficient	Parameters	Units
AD	$S_\mathrm{AD} = \left[\frac{\bar{\nu}_\mathrm{3D}}{4\phi^{\nu_\phi}}\right]$	$\phi, \nu_\phi, \bar{\nu}_\mathrm{3D}$	$\mathrm{m}^3/(\mathrm{mol}\cdot\mathrm{s})$
ER	$S_\mathrm{ER} = \left[\frac{\bar{\nu}_\mathrm{3D}}{4\phi^{\nu_\phi}}\right]$	$\phi, \nu_\phi, \bar{\nu}_\mathrm{3D}$	$\mathrm{m}^3/(\mathrm{mol}\cdot\mathrm{s})$
LH	$S_\mathrm{LH} = \left[\bar{\nu}_\mathrm{2D}\phi^{\frac{3}{2}-\nu_\phi} N_\mathrm{A}^{\frac{1}{2}}\right]$	$\phi, \nu_\phi, \bar{\nu}_\mathrm{2D}, N_\mathrm{A}$	$\mathrm{m}^2/(\mathrm{mol}\cdot\mathrm{s})$

where ϕ is the total surface species molar concentration (including all empty and occupied surface sites), ν_ϕ is the surface concentration exponent equal to the sum of stoichiometric coefficients for all surface reactants on either side of the reaction, $\bar{\nu}_\mathrm{3D}$ is the mean thermal of the incoming reactant for the AD and ER reactions, $\bar{\nu}_\mathrm{2D}$ is the mean thermal speed of the mobile surface species for the LH reaction, and N_A is the Avogadro constant.

4.6.4. Backward reaction rate coefficients for AD reactions

The backward reaction rate coefficient for AD reactions, i.e., the desorption rate coefficient, is often given in the form

$$k_\mathrm{b,AD}(T_\mathrm{w}) = \nu_\mathrm{AD}\, C\, \tilde{T}_\mathrm{w}^{\beta} \exp\left(-\frac{T_\mathrm{c}}{T_\mathrm{w}}\right), \tag{4.15}$$

where ν_{AD} is the attempt frequency in s^{-1} and is taken as a constant in the range 10^{12} to 10^{15} [62], and C, β, and T_{c} are specified for a given reaction model.

4.6.5. Equilibrium constants for non-AD reactions

The relationship between $K_{\mathrm{a},r}$ and G_s^0 can be rewritten as

$$-\ln\left(K_{\mathrm{a},r}\right) RT_{\mathrm{w}} = \left(\sum_{s=1}^{N_s} \nu_s G_s^0(T_{\mathrm{w}})\right)_r . \tag{4.16}$$

For surface reactions, differences in Gibbs free energy between occupied and empty surface sites are required but are not readily available in thermodynamic databases. Marschall et al. [4] introduced a workaround in which these terms are calculated from known forward and backward adsorption/desorption reaction rate coefficients involving the adsorbed surface species of interest.

The workaround can be illustrated with the following example. Consider three generic surface reactions:

- AD: A + E(s) ⇌ A(s), $K_{\mathrm{a,AD}}$ known
- ER: B + A(s) ⇌ AB + E(s), $K_{\mathrm{a,ER}}$ unknown
- LH: A(s) + B(s) ⇌ AB + 2E(s), $K_{\mathrm{a,LH}}$ unknown

then, the relationships between $K_{\mathrm{a},r}$ and G_s^0 for the three reactions are

$$\begin{aligned}
-\ln\left(K_{\mathrm{a,AD}}\right) RT_{\mathrm{w}} &= G^0_{\mathrm{A(s)}} - \left(G^0_{\mathrm{A}} + G^0_{\mathrm{E(s)}}\right), \\
-\ln\left(K_{\mathrm{a,ER}}\right) RT_{\mathrm{w}} &= \left(G^0_{\mathrm{AB}} + G^0_{\mathrm{E(s)}}\right) - \left(G^0_{\mathrm{B}} + G^0_{\mathrm{A(s)}}\right), \\
-\ln\left(K_{\mathrm{a,LH}}\right) RT_{\mathrm{w}} &= \left(G^0_{\mathrm{AB}} + 2G^0_{\mathrm{E(s)}}\right) - \left(G^0_{\mathrm{A(s)}} + G^0_{\mathrm{B(s)}}\right).
\end{aligned} \tag{4.17}$$

Rearranging the three equations yields

$$\begin{aligned} -\ln\left(K_{\mathrm{a,AD}}\right) RT_{\mathrm{w}} &= \left(G^0_{\mathrm{A(s)}} - G^0_{\mathrm{E(s)}}\right) - G^0_{\mathrm{A}}, \\ -\ln\left(K_{\mathrm{a,ER}}\right) RT_{\mathrm{w}} &= \left(G^0_{\mathrm{AB}} - G^0_{\mathrm{B}}\right) - \left(G^0_{\mathrm{A(s)}} - G^0_{\mathrm{E(s)}}\right), \\ -\ln\left(K_{\mathrm{a,LH}}\right) RT_{\mathrm{w}} &= G^0_{\mathrm{AB}} - \left(G^0_{\mathrm{A(s)}} - G^0_{\mathrm{E(s)}}\right) - \left(G^0_{\mathrm{B(s)}} - G^0_{\mathrm{E(s)}}\right). \end{aligned} \tag{4.18}$$

Values of G^0_{A}, G^0_{B}, and G^0_{AB} are known from thermodynamic databases and the difference $\left(G^0_{\mathrm{A(s)}} - G^0_{\mathrm{E(s)}}\right)$ can be obtained from the AD reaction and substituted into the ER and LH reactions. Similarly, $\left(G^0_{\mathrm{B(s)}} - G^0_{\mathrm{E(s)}}\right)$ can be derived from an AD reaction involving $G^0_{\mathrm{B(s)}}$.

4.6.6. Loss efficiency for volume species

For a volume species s, the loss efficiency λ_s is defined as the fraction of the collisions with the surface that result in the volume species being consumed in a surface reaction

$$\lambda_s = \frac{-\dot{\omega}_s^{(\mathrm{s})}}{\Gamma_s}. \tag{4.19}$$

Although the loss efficiency is formulated identically as the recombination efficiency for a volume species s, they are used differently in this thesis: the recombination efficiency denotes an input to the partially catalytic model, and the loss efficiency represents an output from the finite-rate surface chemistry model.

Chapter 5. Results

Presented in this chapter are four test cases intended for the verification and validation of the correct implementations of the surface catalycity models.

1. The steady-state three-dimensional Electre test case is employed to verify and validate the implementation of the partially catalytic boundary condition.
2. A zero-dimensional reactor with one irreversible adsorption reaction is considered to validate the spatial assembly of volume species mass residuals as well as the temporal integration of surface species concentrations for the finite-rate surface chemistry model.
3. A zero-dimensional reactor with reversible AD, ER, and LH reactions is studied to verify the computation of forward and backward surface reaction rate coefficients within the finite-rate surface chemistry model.
4. The steady-state test case of a reacting air flow around a two-dimensional cylinder with a catalytic silica surface is intended to demonstrate gas composition predictions using the finite-rate surface chemistry model.

5.1. Electre test case

Verification and validation of the correct implementation of the partially catalytic boundary condition for species concentrations are conducted using the Electre test case. Electre is a blunt spherical-conical body with a total length $L = 0.4$ m, a leading-edge radius of 0.035 m, and a cone angle of 4.6 degrees. Electre was tested in two high-enthalpy facilities, namely the ONERA hot-shot F4 and the DLR Stalker tube HEG [63–65]. The HEG test conditions [66] are recalled in Table 5.1 and serve as initial and boundary conditions for all subsequent simulations.

Table 5.1. Flow conditions for the Electre test case.

Quantity	Symbol	Value
Freestream Mach number	Ma_∞	9.7
Freestream Reynolds number	Re_∞	1.1×10^5
Overall Knudsen number	$\mathrm{Kn}_{\mathrm{ov}}$	1.3×10^{-4}
Freestream velocity	u_∞	5,919 m/s
Freestream density	ρ_∞	1.64×10^{-3} kg/m^3
Freestream pressure	p_∞	430 Pa
Freestream temperature	T_∞	790 K
Freestream N mass fraction	y_{N}	0
Freestream O mass fraction	y_{O}	0.179
Freestream N_2 mass fraction	$y_{\mathrm{N_2}}$	0.752
Freestream O_2 mass fraction	$y_{\mathrm{O_2}}$	0.036
Freestream NO mass fraction	y_{NO}	0.033
Wall temperature	T_{w}	300 K

Two grids are utilized to solve the Electre test case. The 95 × 100 × 360 structured mesh shown in Figure 5.1 with a 90 × 90 patch on the spherical nose is composed of 2.6 M nodes and 2.5 M elements, with a Y^+ value of 0.025 and a geometric progression ratio of 1.1. The mesh presented in Figure 5.2 is obtained with OptiGrid [59] after four optimization cycles based on density, pressure, temperature, and the velocity components. The initial unstructured mesh contains 340 k nodes and 860 k elements, including 20 prism layers, and a Y^+ value of 0.15 and the same geometric progression ratio. Mesh optimization is conducted on the volume and surfaces at the exception of the prism layers on the surface. The adaptation is configured with a 4 M node target and a maximum of 20 M nodes and 40 M elements. The minimum and maximum edge lengths are set to 5×10^{-5} m and 0.3 m, respectively. Within each cycle, twelve adaptation iterations each consisting of one refinement-coarsening operation are sandwiched by 20 and 200 node movements, and then

followed by five edge swapping iterations. The final adapted mesh for the fully catalytic run has 4.1 M nodes and 11.0 M elements.

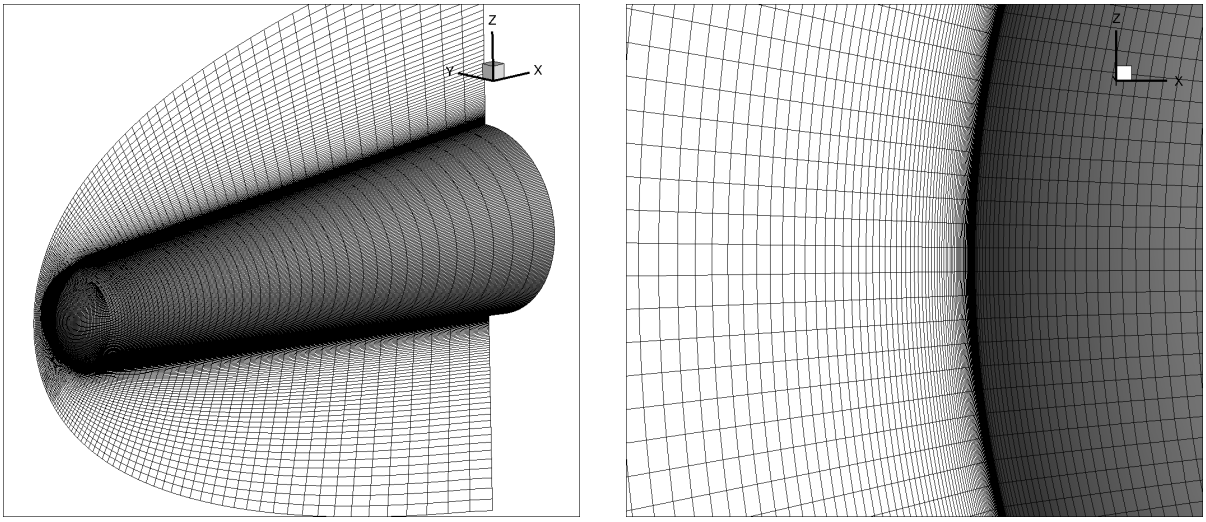

(a) Global view of the mesh **(b) Magnified view of the spherical nose**

Figure 5.1. Structured mesh used to simulate the fully catalytic Electre body.

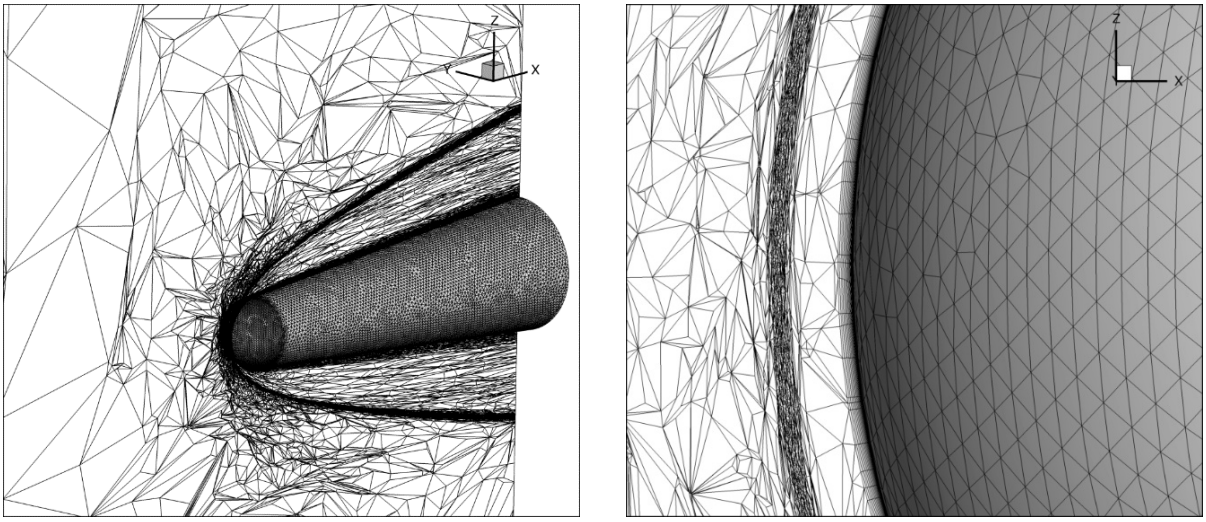

(a) Global view of the mesh **(b) Magnified view of the spherical nose**

Figure 5.2. Adapted unstructured mesh used to simulate the fully catalytic Electre body.

The HALO3D results are obtained with a second-order accurate Roe scheme [56] and the van Albada slope limiter [67]. Laminar flow is considered as the freestream Reynolds number is well below the laminar to turbulent transition threshold suggested by the AEDC wind tunnel data for $\mathrm{Ma}_\infty = 10$ [68]. The flow is assumed to be in thermal equilibrium, and the thermally perfect gas properties are calculated using polynomials published by NASA [47]. Five species and 17 reactions from Park's 1993 model [69] are considered for the volume chemistry and are recalled in Appendix A.2.

A baseline simulation "*HALO3D nc*" is run using a noncatalytic isothermal wall maintained at a temperature of 300 K. A second simulation labeled as "*HALO3D fc*" employs a fully catalytic isothermal wall boundary condition, while a third simulation tagged as "*HALO3D pc*" uses a partially catalytic isothermal wall boundary condition with two constant recombination efficiencies $\gamma_\mathrm{N} = \gamma_\mathrm{O} = 0.005$ and $\gamma_\mathrm{N} = \gamma_\mathrm{O} = 0.05$ being employed. The noncatalytic and fully catalytic simulations are run on both the structured and unstructured meshes, while the partially catalytic simulation is only performed with the unstructured mesh.

Contour plots of the *x*-component of the velocity vector and temperature for the structured and unstructured fully catalytic runs are shown in Figure 5.3 and Figure 5.4, respectively. The maximum static temperature experience across the bow shock is approximately 1,000 K higher for the adapted unstructured grid than for the structured grid, indicating that the shock discontinuity is better resolved by the adapted grid.

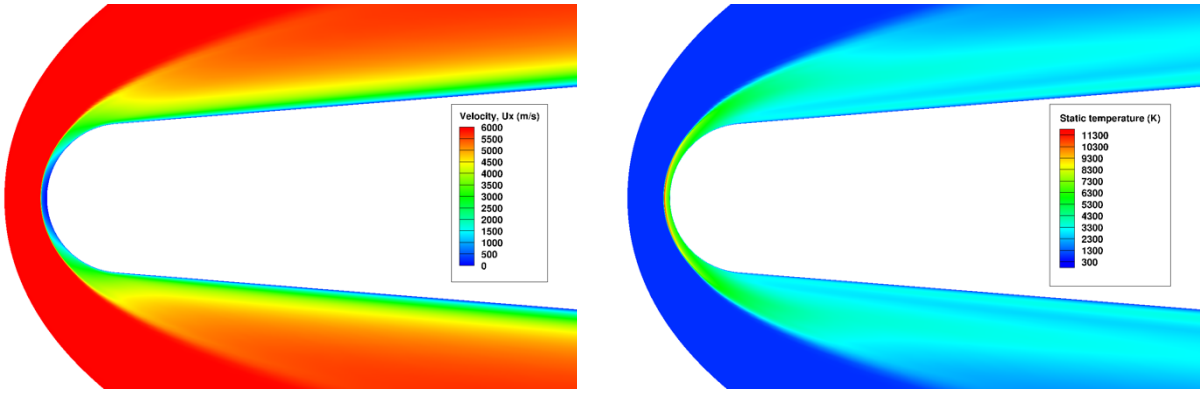

(a) *x*-component of the velocity vector **(b) Temperature**

Figure 5.3. Contour plots in the *xz*-plane for the structured fully catalytic Electre test case.

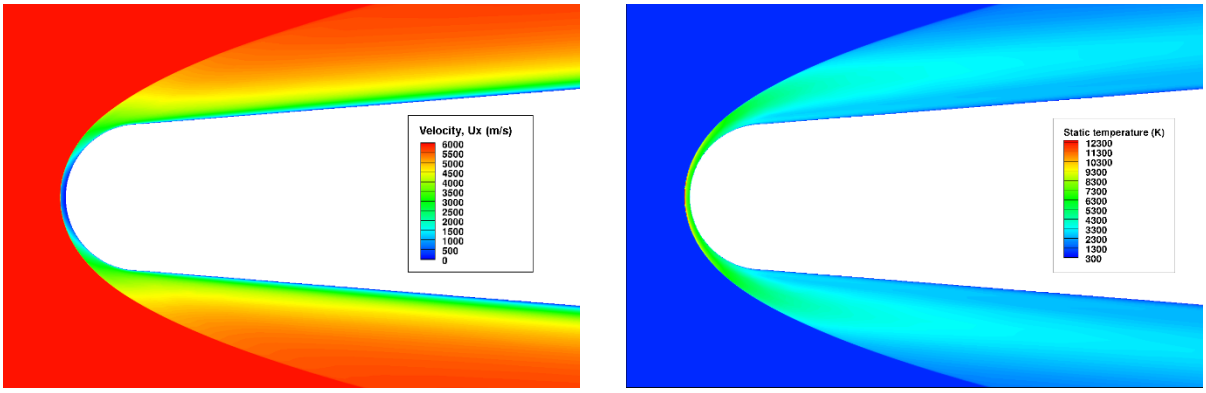

(a) *x*-component of the velocity vector **(b) Temperature**

Figure 5.4. Contour plots in the *xz*-plane for the adapted unstructured fully catalytic Electre test case.

In Figure 5.5, velocity magnitude, temperature, density, and species mass fractions stagnation line profiles are presented for the unstructured grid. The velocity magnitude, temperature, and mixture density profiles are nearly superimposed for the noncatalytic and fully catalytic cases. Both cases exhibit a shock standoff distance of 2.8 mm, and a maximum temperature of 12,300 K along the stagnation line.

The stagnation line qualities in the post-shock region (approx. between stagnation line positions of -2.5 and -1.5 mm) are continuous, smooth, and gradually sloped, hence as expected, OptiGrid significantly reduced the number of nodes. The absence of oscillations in the contours indicates that the grid is sufficiently fine to accurately resolve the flow and chemistry quantities in the post-shock region. Additionally, as shown by Gao et al. [60], the accuracy of the surface heat flux depends mainly on the resolution of the shock. The shock is well resolved in the adapted unstructured grid, meaning that the maximum error estimate is sufficiently small, and the grid is adequately fine within the shock. By extension of the error equi-distribution, the grid is reasonably fine in the post-shock region.

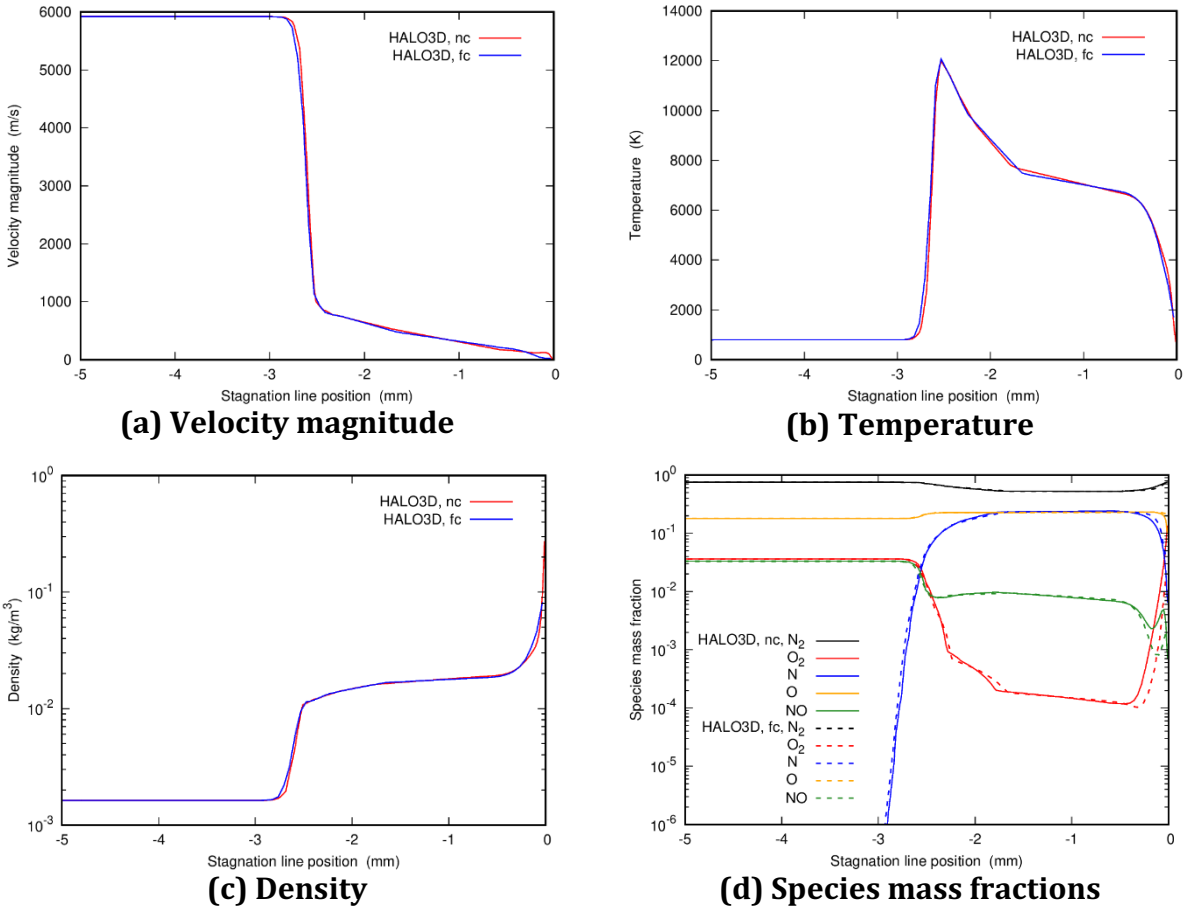

Figure 5.5. Stagnation line quantities for the noncatalytic and fully catalytic unstructured HALO3D runs of the Electre test case.

In Figure 5.6, the surface pressure coefficient is plotted in the *xz*-plane as a function of the normalized *x*-coordinate position. The pressure coefficient profiles for all HALO3D runs are superimposed with the solutions given by Fluent [66]. They are also closely matching the experimental data points on the spherical region but are slightly lower than the experimental values on the conical region. The differences with the experimental data can be attributed to the aft body of the Electre not being modeled in both HALO3D and Fluent simulations. The simulation results show that the mesh type and surface chemistry do not have a significant influence on the pressure coefficient.

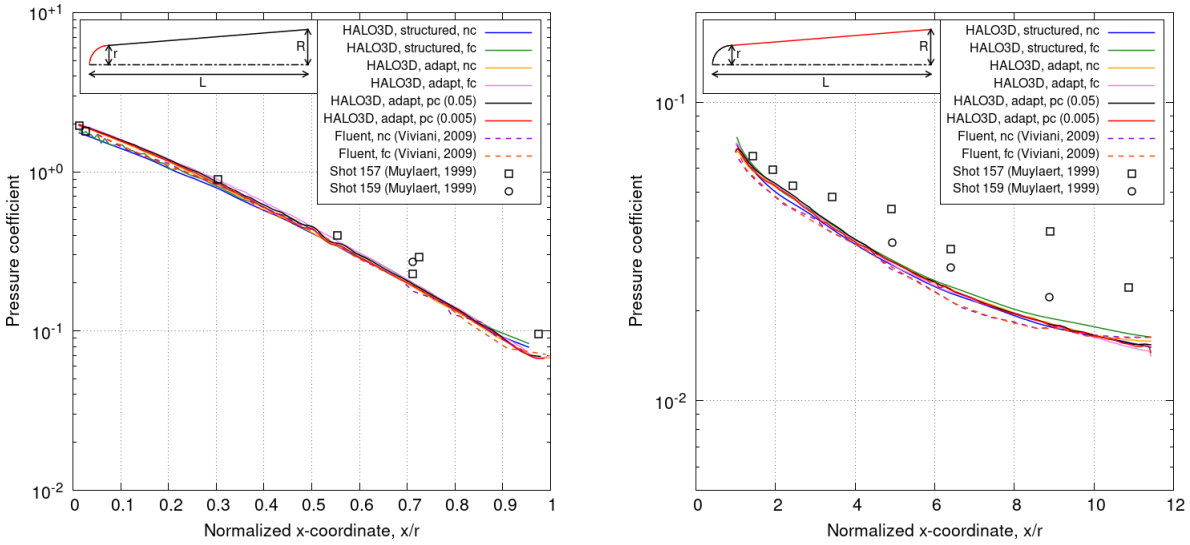

(a) Spherical region **(b) Conical region**

Figure 5.6. Surface pressure coefficient for the Electre test case.

In Figure 5.7, the surface heat flux is plotted in the *xz*-plane as a function of the normalized *x*-coordinate position. As anticipated, the noncatalytic and the fully catalytic results provide the lower and upper bounds of the heat flux, respectively, and the increasing recombination efficiencies of the various catalytic models cause greater heat flux on the surface.

Regarding the unstructured HALO3D simulations, the noncatalytic model underestimates the wall heat flux at the rear of the spherical region and at the conical region compared to experimental results. Conversely, the fully catalytic heat flux profiles obtained from HALO3D and Fluent are in good agreement. Both curves are reasonably close to experimental values on the spherical region but overpredict those on the conical region. The heat flux profiles for the partially catalytic runs with $\gamma_N = \gamma_O = 0.005$ and $\gamma_N = \gamma_O = 0.05$ are shown to tightly bracket experimental results, with the front of the conical region matching the higher γ value and the rear resembling the lower γ value.

While the fully catalytic heat flux profile of the HALO3D structured run appears to closely match the experimental data, the values should be considered inaccurate as the fully catalytic

model is expected to overpredict the heat flux. The discrepancy is likely caused by the lower peak temperature across the shock for the HALO3D structured run which contributes to lower temperatures in the region after the shock and lower heat flux at the wall. The accuracy of the heat flux estimation is degraded by a structured mesh that is poorly aligned with the shock, therefore demonstrating the benefit of using an anisotropic mesh optimization tool for accurate surface heat flux predictions.

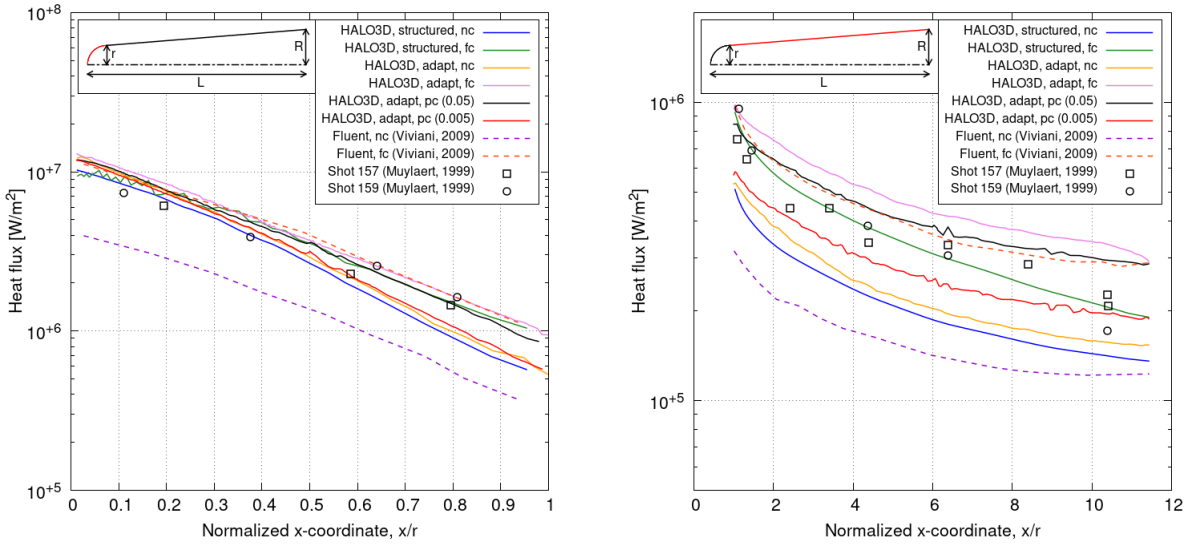

(a) Spherical region **(b) Conical region**

Figure 5.7. Surface heat flux for the Electre test case.

The algorithm of OptiGrid aims to equally distribute the error estimate in the metric space, thus when not constrained by minimum/maximum allowable edge lengths and with sufficient mesh manipulation operations, the optimized grid should have similar error estimates in the metric space. The additional refinement of the post-shock region can be achieved either by reducing the maximum allowable error estimate, which would induce a global refinement, or by significantly reducing the maximum allowable edge length, which would greatly refine the freestream region. Both methods will result in significant increases in the number of nodes in return for small amount of additional refinement in the post-shock region.

The process of grid optimization is similar to a grid-convergence study in the sense that better results can be produced using successively adapted meshes. Two characteristics of OptiGrid are demonstrated by Dompierre et al. [70]: First, directional flow features such as shocks and wakes are better resolved with more adaptation cycles but with diminishing marginal returns. Second, with identical settings and enough adaptation cycles, drastically different initial meshes will evolve into nearly identical final meshes. Together, the two characteristics signify that with sufficient adaptation cycles, the final adapted mesh will be close to optimal for a given number of nodes and elements, which cannot be shown for the case of systematic mesh refinement and extrapolation to the limit. For the Electre test case, as with most cases with OptiGrid, an optimal grid is reached by the third or fourth cycle.

5.2. Reactor with one irreversible adsorption reaction

The spatial assembly of volume species mass residuals as well as the temporal integration of surface species concentrations for the finite-rate surface chemistry model are validated with a zero-dimensional reactor with one irreversible adsorption reaction. The reactor consists of a 1m × 1m × 1m cube discretized into 4 × 4 × 4 hexahedron elements. One of the six faces of the domain has the no-slip isothermal finite-rate surface chemistry boundary condition applied, while the remaining five have slip wall boundary conditions.

The pressure is constant at 100 Pa, while the volume temperature and reacting surface temperature are both constant at 3000 K. The volume gas composition is fixed, containing only atomic nitrogen, and there are no volume reactions. Empty surface sites E(s) and surface atomic nitrogen N(s) are present on the reacting surface, with an initial molar concentration of 10^{-6} mol/m^2 for E(s) and 0 mol/m^2 for N(s). The adsorption reaction occurring at the surface is N + E(s) → N(s), with reaction rate coefficient parameters of $C_{\mathrm{AD}} = 0.05$, $\beta = 0$, and $T_{\mathrm{c,AD}} = 0$ K.

An analytical solution for the transient response of the molar concentration of both surface species can be derived because of the constant molar concentration of N and the simplicity of the surface reacting kinetics. Using the conservation of the total molar concentration of surface species

$$\phi = \phi_{\mathrm{E(s)}} + \phi_{\mathrm{N(s)}}, \tag{5.1}$$

the molar production rate of N(s) can be given by

$$\begin{aligned} \frac{\mathrm{d}\phi_{\mathrm{N(s)}}}{\mathrm{d}t} &= \left(\nu''_{\mathrm{N(s)}} - \nu'_{\mathrm{N(s)}}\right)\left(k_{\mathrm{f}} c_{\mathrm{N}}^{\nu'_{\mathrm{N}}} \phi_{\mathrm{E(s)}}^{\nu'_{\mathrm{E(s)}}} - k_{\mathrm{b}} \phi_{\mathrm{N(s)}}^{\nu''_{\mathrm{N(s)}}}\right), \\ &= k_{\mathrm{f}} c_{\mathrm{N}} \phi_{\mathrm{E(s)}} = k_{\mathrm{f}} c_{\mathrm{N}}\left(\phi - \phi_{\mathrm{N(s)}}\right). \end{aligned} \tag{5.2}$$

The molar production rate equation can be rewritten as a first order ordinary differential equation

$$\frac{\mathrm{d}x(t)}{\mathrm{d}t} = k(a - x(t)), \tag{5.3}$$

where $a = \phi$, $k = k_{\mathrm{f}} c_{\mathrm{N}}$, $x(t) = \phi_{\mathrm{N(s)}}$, and with the initial condition of $x(t = 0) = 0$. The solution to the ordinary differential equation is given as

$$x(t) = a\,(1 - \exp(-kt)). \tag{5.4}$$

Therefore, the analytical solutions for E(s) and N(s) are given as

$$\begin{aligned} \phi_{\mathrm{E(s)}}(t) &= \phi \exp\left(-k_f c_{\mathrm{N}} t\right), \\ \phi_{\mathrm{N(s)}}(t) &= \phi\left(1 - \exp\left(-k_f c_{\mathrm{N}} t\right)\right). \end{aligned} \tag{5.5}$$

The transient response of the surface coverage of N(s) from HALO3D is plotted against the analytical expression in Figure 5.8. In the simulation, a uniform physical timestep of 10^{-7}

seconds is adequately short to accurately capture the initial evolution of the surface coverage and a total simulation time of 10^{-4} seconds is sufficiently long for the surface chemistry to reach equilibrium, i.e., when surface coverage of N(s) approaches unity. The simulation results are in complete agreement with the analytical solution, validating the spatial assembly of volume species mass residuals as well as the temporal integration of surface species concentrations for the finite-rate surface chemistry model.

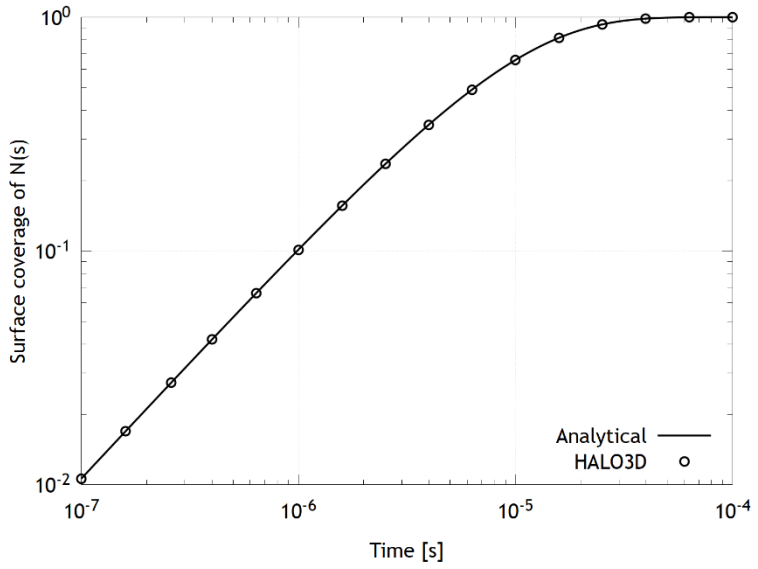

Figure 5.8. Transient response of the surface coverage of N(s) with one irreversible adsorption reaction.

5.3. Reactor with reversible AD, ER, and LH reactions

The computation of forward and backward surface reaction rate coefficients within the finite-rate surface chemistry model is verified through a zero-dimensional reactor with reversible AD, ER, and LH reactions. In particular, it is imperative to ensure the correct implementation of the workaround to compute equilibrium constants and backward reaction rate coefficients for non-AD reactions as described in Chapter 4.6.5. The reactor consists of a 1m × 1m × 1m cube represented by a single hexahedron element. Since the spatial distribution of surface species is not of interest in this case, a single element is

sufficient. One of the six faces of the domain has the no-slip isothermal finite-rate surface chemistry boundary condition applied, while the remaining five have slip wall boundary conditions.

Three fixed pressure values are explored: 200, 2000, and 20000 Pa, while the constant volume temperature and reacting surface temperature vary from 500 to 3500 K. The volume conditions are fixed, containing atomic oxygen and molecular oxygen with constant molar fractions of 0.1 and 0.9 respectively, and no volume reactions. Empty surface sites E(s) and surface atomic oxygen O(s) are present on the surface, with an initial molar concentration of 7.5×10^{-6} mol/m^2 for E(s) and 0 mol/m^2 for O(s). Three reversible surface reactions of different types can occur, and their reaction parameters are presented in Table 5.2. $\beta = 0$ for all three reactions and $C_{\mathrm{AD,b}} = 1$ for the desorption reaction.

Table 5.2. Surface reactions for the reactor with reversible AD, ER, and LH reactions

No.	Reaction	Type	Coefficient	T_c [K]
1f	O + E(s) ⇌ O(s)	AD,f	$C_{\mathrm{AD,f}} = 0.05$	0
1b	O(s) ⇌ O + E(s)	AD,b	$\nu_{\mathrm{AD}} = 10^{12}$ s^{-1}	42095
2	O + O(s) ⇌ O_2 + E(s)	ER	$C_{\mathrm{ER}} = 0.001$	1082
3	2O(s) ⇌ O_2 + 2E(s)	LH	$C_{\mathrm{LH}} = 0.1$	36082

As per the workaround, the unknown Gibbs free energy of O(s) is derived from the known forward and backward reaction rate coefficients of the AD reaction, and then substituted into the ER and LH reactions to calculate equilibrium constants and backward reaction rate coefficients. Therefore, it is of paramount importance to use the same thermodynamic database as Marschall et al. [4] to compute Gibbs free energies of volume species.

The Gibbs free energies of O, O_2, and O(s) as a function of temperature is displayed in Figure 5.9. Also shown in this Figure is $-\ln\left(K_{\mathrm{a,AD}}\right) RT$, which is part of the formula that calculates $G^0_{\mathrm{O(s)}}$ and has the same units and a similar order of magnitude as the Gibbs free energies of

the other species. Since Gibbs free energies are often negative and negative values cannot be plotted on logarithmic scales, the negative portions are inverted and plotted with dashed lines while the positive portions remain in solid lines. $G^0_{O_2}$, $G^0_{O(s)}$, and $-\ln\left(K_{a,AD}\right)RT$ are negative throughout the range of temperature of interest, while G^0_O transitions from positive to negative at around 1400 K. This Figure should prove valuable to future researchers implementing a finite-rate surface chemistry module, as it was not provided by prior authors investigating this case.

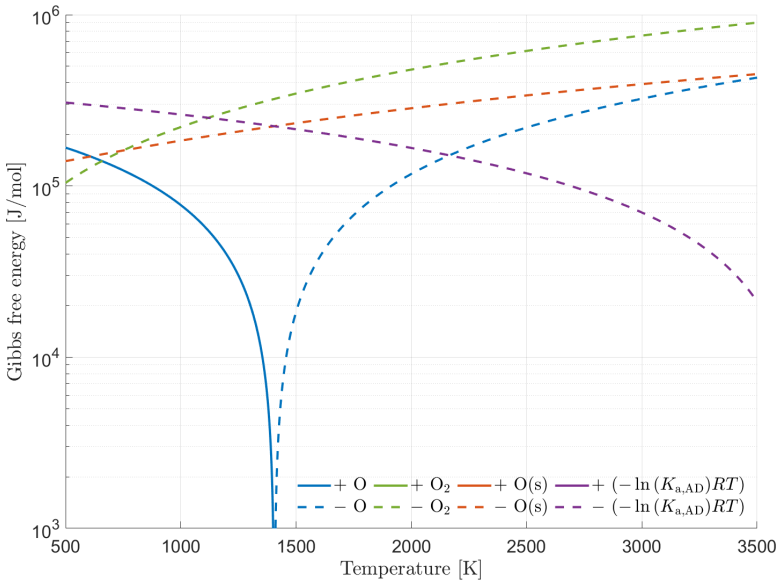

Figure 5.9. Gibbs free energies of O, O_2, and O(s) vs. temperature.

The forward and backward reaction rate coefficients and the concentration-based equilibrium constants for the three surface reactions are presented in Figure 5.10. For AD and ER reactions, the forward rate coefficients remain several orders of magnitude higher than the backward rate coefficients until around 3500 K where the forward rate coefficients are surpassed by the backward rate coefficients. Additionally, the forward rate coefficient of the AD reaction remains higher than that of the ER reaction throughout the temperature range. For the LH reaction, the opposite trend is observed where the backward rate coefficient is higher than the forward rate coefficient until around 3000 K where the two coefficients switch. Except for the forward rate coefficients of the AD and ER reactions, all

reaction rate coefficients and equilibrium constants exhibit a strong temperature dependency. This Figure has also not been provided by prior authors investigating this case and should prove valuable to future researchers.

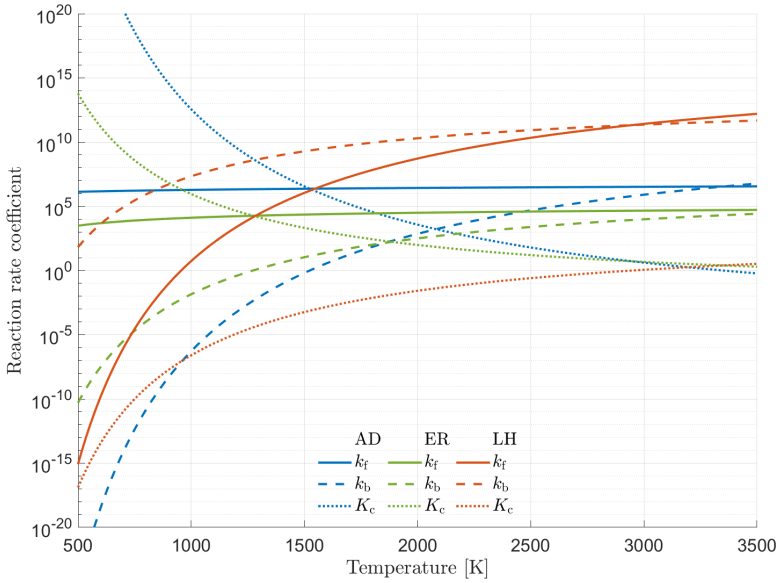

Figure 5.10. Reaction rate coefficients and equilibrium constants vs. temperature for reversible AD, ER, and LH reactions.

The analytical solution for the surface concentration of O(s) at equilibrium is given by

$$\phi_{\mathrm{O(s)}} = \frac{2c}{-b + \sqrt{b^2 - 4ac}}, \tag{5.6}$$

where the coefficients a, b, and c are calculated based on the forward and backward rate coefficients of the surface reactions. This form of the quadratic formula is employed instead of the usual form with $2a$ as the denominator due to the better stability in the lower temperature range for the present values of the coefficients. With all three surface reactions active, a, b, and c are given by [4]

$$\begin{aligned} a &= -2k_{\mathrm{f,LH}} + 2k_{\mathrm{b,LH}}c_{\mathrm{O_2}}, \\ b &= -k_{\mathrm{f,AD}}c_{\mathrm{O}} - k_{\mathrm{b,AD}} - k_{\mathrm{f,ER}}c_{\mathrm{O}} - k_{\mathrm{b,ER}}c_{\mathrm{O_2}} - 4k_{\mathrm{b,LH}}c_{\mathrm{O_2}}\phi, \\ c &= +k_{\mathrm{f,AD}}c_{\mathrm{O}}\phi + k_{\mathrm{b,ER}}c_{\mathrm{O_2}}\phi + 2k_{\mathrm{b,LH}}c_{\mathrm{O_2}}\phi^2. \end{aligned} \tag{5.7}$$

The surface coverage of O(s) from HALO3D is plotted against the values presented by Marschall et al. [4] in Figure 5.11 in both linear and logarithmic scales. Below 1500 K, the forward AD reaction, which produces O(s), is dominant and the surface coverage of O(s) remains close to one. Above 1500 K, the forward LH reaction, which consumes O(s), is the defining reaction and the surface coverage decreases linearly on a logarithmic scale as temperature increases. At lower pressures, the surface coverage starts to decrease at lower temperatures, since the forward AD reaction rate depends on the concentration of the volume-phase O, which is pressure-dependent. Conversely, the forward LH reaction rate depends on the concentration of the surface-phase O(s), which is pressure-independent.

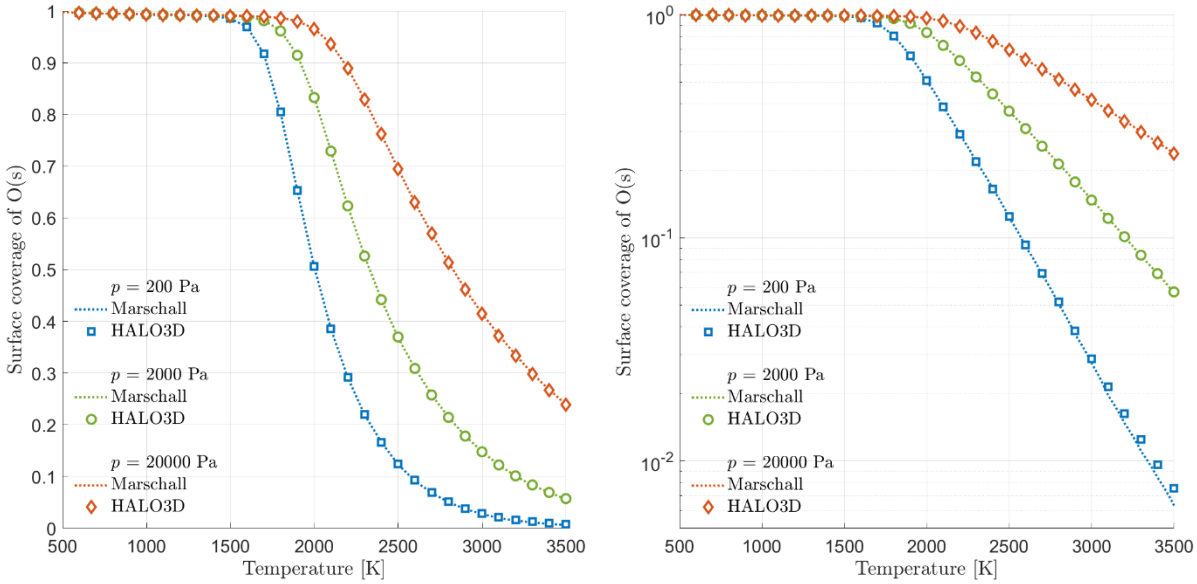

(a) Linear scale **(b) Logarithmic scale**

Figure 5.11. Surface coverage of O(s) vs. temperature with reversible AD, ER, and LH reactions.

Once the molar concentrations of the surface species are known, the loss efficiencies can be calculated. Their analytical expressions at equilibrium when all three surface reactions are active are given by [4]

$$\begin{aligned}
\lambda_{\mathrm{O}} &= \frac{-\dot{\omega}_{\mathrm{O}}^{(\mathrm{s})}}{\Gamma_{\mathrm{O}}} \\
&= -\frac{1}{\Gamma_{\mathrm{O}}}\left(-k_{\mathrm{f,AD}} c_{\mathrm{O}} \phi_{\mathrm{E(s)}} + k_{\mathrm{b,AD}} \phi_{\mathrm{O(s)}}\right. \\
&\quad \left. - k_{\mathrm{f,ER}} c_{\mathrm{O}} \phi_{\mathrm{O(s)}} + k_{\mathrm{b,ER}} c_{\mathrm{O_2}} \phi_{\mathrm{E(s)}}\right), \\
\lambda_{\mathrm{O_2}} &= \frac{-\dot{\omega}_{\mathrm{O_2}}^{(\mathrm{s})}}{\Gamma_{\mathrm{O_2}}} \\
&= -\frac{1}{\Gamma_{\mathrm{O_2}}}\left(+k_{\mathrm{f,ER}} c_{\mathrm{O}} \phi_{\mathrm{O(s)}} - k_{\mathrm{b,ER}} c_{\mathrm{O_2}} \phi_{\mathrm{E(s)}}\right. \\
&\quad \left. + k_{\mathrm{f,LH}} \phi_{\mathrm{O(s)}}^2 - k_{\mathrm{b,LH}} c_{\mathrm{O_2}} \phi_{\mathrm{E(s)}}^2\right).
\end{aligned} \tag{5.8}$$

Figure 5.12 shows the loss efficiencies of O and O_2 with three different reaction models: all three reactions active (solid blue line), AD and ER only (dotted green line), and AD and LH only (dashed orange line). λ_O is dictated by the ER mechanism at low temperatures and the LH mechanism at mid temperatures, whereas λ_{O_2} is completely dominated by the LH mechanism. The loss efficiencies with all three reactions active equal to the sum of AD and ER only and AD and LH only.

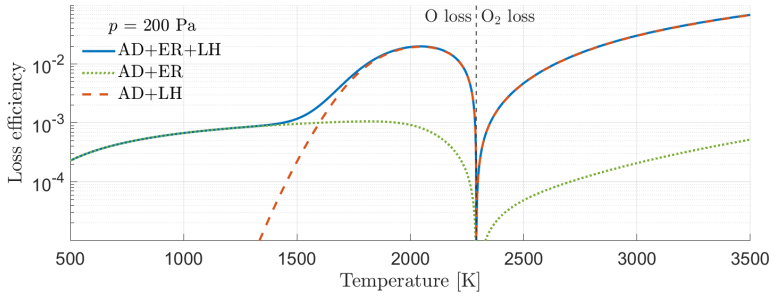

(a) $p = 200$ Pa

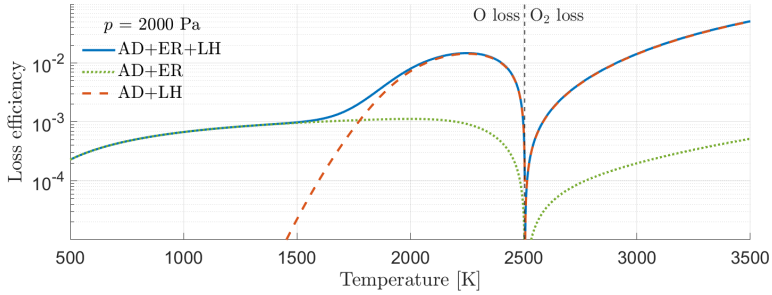

(b) $p = 2000$ Pa

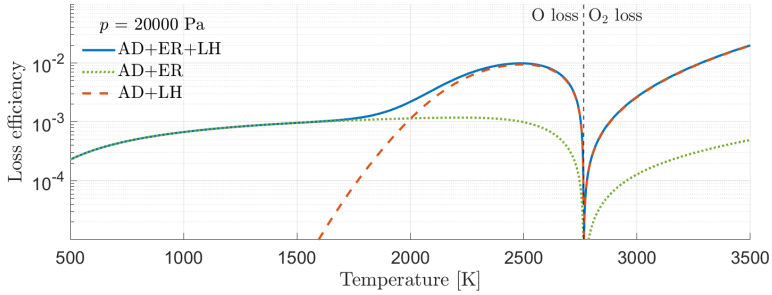

(c) $p = 20000$ Pa

Figure 5.12. Loss efficiencies of O and O_2 vs. temperature with three different reaction models.

The loss efficiencies of O and O_2 given by HALO3D are plotted against the values presented by Marschall et al. [4] in Figure 5.13. Four characteristic regimes exist as a function of temperature. In the lowest temperature range, λ_O gradually increases and is controlled by the forward ER reaction. In the lower-middle temperature range, the dominant forward LH reaction frees up empty surface sites and thus allows more O to be adsorbed, driving λ_O to increase rapidly towards a peak. In the higher-middle temperature range, the now higher dissociative backward ER and LH reaction rates effectively counter the combinative forward reaction rates, causing λ_O to drop sharply to zero. In the highest temperature range, the dissociative backward ER and LH reactions are dominant, and λ_O is replaced by λ_{O_2}, which also increases with temperature.

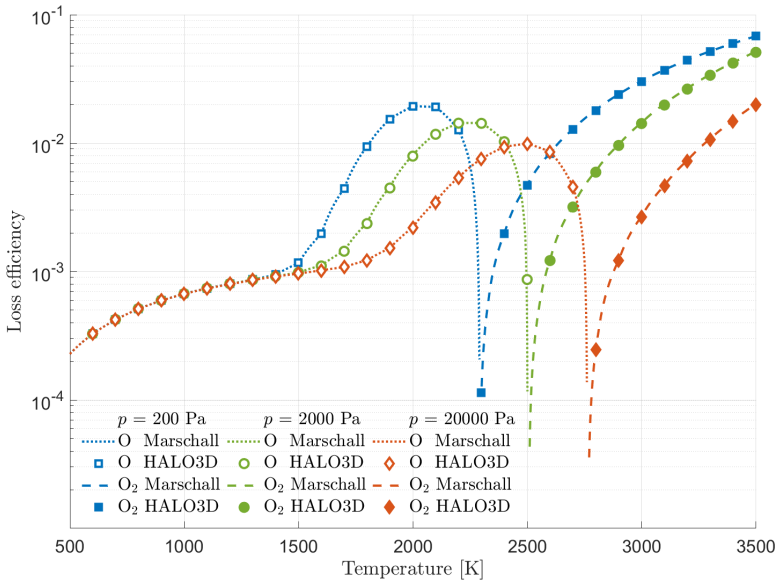

Figure 5.13. Loss efficiencies of O and O_2 vs. temperature with reversible AD, ER, and LH reactions.

The HALO3D equilibrium solutions of surface coverage of O(s) and loss efficiencies of O and O_2 show an excellent match with the values of Marschall et al. [4]. The only discrepancies appear for the surface coverage at 200 Pa above 3000 K which can be attributed to inaccuracies from the digitalization of the reference figure in linear scale and exaggerated by the logarithmic scale. Furthermore, since the distinct behaviors of the loss efficiencies in the

four temperature regions are a consequence of the competing effects of the forward and backward ER and LH reactions, the perfect agreement with the reference values indicates the accurate characterization of all reaction rate coefficients and the correct implementation of the workaround. Therefore, the implementation of the forward and backward surface reaction rate coefficients within the finite-rate surface chemistry model has been verified.

The HALO3D results for the Gibbs free energies of O, O_2, and O(s), the reaction rate coefficients and equilibrium constants for reversible AD, ER, and LH reactions, and the surface concentrations of O(s) with all three reactions are organized in Appendix A.3. These tabulated data should enable future researchers investigating this case to reconstruct the remaining surface concentrations and loss efficiencies to be used as reference values.

5.4. Reacting air flow around a cylinder with a catalytic silica surface

Computations of the volume and surface species composition at the wall are showcased using a steady-state test case of a reacting air flow around a two-dimensional cylinder with a catalytic silica surface. The domain surrounding the forebody of the two-meter-diameter cylinder is discretized using a 120×200 structured mesh shown in Figure 5.14, composed of 24.3 k nodes and 24.0 k quadrilateral elements, with a Y^+ value of 1.0 and a geometric progression ratio of 1.1. The surface of the cylinder has the no-slip isothermal boundary condition applied.

The flow conditions of the cylinder test case used in simulations by various codes are recalled in Table 5.3 [5–7]. The HALO3D results are obtained with a second-order accurate Roe scheme [56] and the van Albada slope limiter [67]. Laminar flow is considered as the freestream Reynolds number is well below the laminar to turbulent transition threshold suggested by the flight test data for $\mathrm{Ma}_\infty = 20$ [71]. The flow is assumed to be in thermal equilibrium, and the thermally perfect gas properties are calculated using polynomials

published by NASA [47]. Five species and 17 reactions from Park's 1993 model [69] are considered for the volume chemistry and are recalled in Appendix A.2.

Figure 5.14. Structured mesh for the cylinder test case.

Table 5.3. Flow conditions for the cylinder test case.

Quantity	Symbol	Value
Freestream Mach number	Ma_∞	21.16
Freestream Reynolds number	Re_∞	4.5×10^5
Overall Knudsen number	$\mathrm{Kn}_{\mathrm{ov}}$	6.9×10^{-5}
Freestream velocity	u_∞	6,000 m/s
Freestream density	ρ_∞	1.0×10^{-3} kg/m^3
Freestream pressure	p_∞	57.54 Pa
Freestream temperature	T_∞	200 K
Freestream N mass fraction	y_{N}	0
Freestream O mass fraction	y_{O}	0
Freestream N_2 mass fraction	$y_{\mathrm{N_2}}$	0.79
Freestream O_2 mass fraction	$y_{\mathrm{O_2}}$	0.21
Freestream NO mass fraction	y_{NO}	0
Wall temperature	T_{w}	2250 K

The finite-rate surface chemistry model for the air and silica system involves empty surface sites E(s), surface atomic nitrogen N(s), and surface atomic oxygen O(s) on the surface, with an initial molar concentration of 7.5×10^{-6} mol/m^2 for E(s) and 0 mol/m^2 for both N(s) and O(s). Additionally, nine surface reactions are considered, accounting for the adsorption of nitrogen and oxygen atoms and the recombination through ER and LH mechanisms. The parameters for the surface reactions are listed in Table 5.4 and the equilibrium constants and the backward reaction rate coefficients of the ER and LH reactions are computed using the workaround as described in Chapter 4.6.5.

Table 5.4. Surface reactions for the air and silica system.

No.	Reaction	Type	Coefficient	T_c [K]
1f	N + E(s) ⇌ N(s)	AD,f	$C_{\mathrm{AD,f}} = 0.05$	0
2f	O + E(s) ⇌ O(s)	AD,f	$C_{\mathrm{AD,f}} = 0.05$	0
1b	N(s) ⇌ N + E(s)	AD,b	$\nu_{\mathrm{AD}} = 10^{12}$ s^{-1}	42095
2b	O(s) ⇌ O + E(s)	AD,b	$\nu_{\mathrm{AD}} = 10^{12}$ s^{-1}	42095
3	N + N(s) ⇌ N_2 + E(s)	ER	$C_{\mathrm{ER}} = 0.001$	1082
4	O + O(s) ⇌ O_2 + E(s)	ER	$C_{\mathrm{ER}} = 0.001$	1082
5	N + O(s) ⇌ NO + E(s)	ER	$C_{\mathrm{ER}} = 0.001$	1082
6	O + N(s) ⇌ NO + E(s)	ER	$C_{\mathrm{ER}} = 0.001$	1082
7	2N(s) ⇌ N_2 + 2E(s)	LH	$C_{\mathrm{LH}} = 0.1$	36082
8	2O(s) ⇌ O_2 + 2E(s)	LH	$C_{\mathrm{LH}} = 0.1$	36082
9	N(s) + O(s) ⇌ NO + 2E(s)	LH	$C_{\mathrm{LH}} = 0.2$	36082

A two-step process is used to compute the steady-state solution with surface catalycity in HALO3D: first, the steady-state baseline solution is obtained using the noncatalytic wall; then, the steady-state catalytic solution is calculated, restarting from the baseline but employing the finite-rate surface chemistry boundary condition instead.

The species mass fractions of N, O, and NO along the stagnation line from the catalytic solution of HALO3D are compared against the DPLR results [5] in Figure 5.15. N, O, and NO are products of dissociation and exchange reactions involving N_2 and O_2 in the post shock region. Away from the wall, y_N and y_O are similar in magnitude with a very low y_{NO}. Closer to the wall, y_N decreases steadily towards zero at -0.5 mm, y_O remains nearly constant but begins to drop at -1.0 mm, y_{NO} remains low. The simulation and reference values of y_O and y_{NO} are in good accord throughout, and the values of y_N near the wall are also well matched. The differences for y_N away from the wall are likely due to discrepancies in the noncatalytic solutions. Important settings including mesh parameters and the volume chemistry model are not provided in the reference, potentially causing mismatches in the setup between the two solvers, contributing to the different solutions.

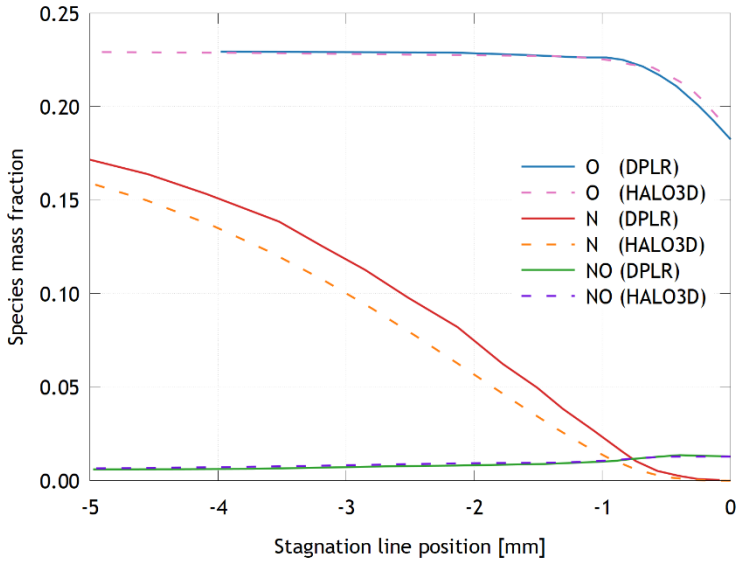

Figure 5.15. Species mass fractions of N, O, and NO along the stagnation line for the cylinder test case.

The surface coverage of E(s), N(s), and O(s) from the catalytic solution of HALO3D is plotted against the DPLR results [5] in Figure 5.16. Within 30 deg from the stagnation point, the catalytic surface is dominated by O(s) complemented by a small amount of E(s). As the angle increases past 30 deg, O(s) are gradually replaced by E(s) and the surface concentrations of

the two species become similar at 90 deg. The surface coverage of N(s) is negligible below 50 deg and remains low in the remaining range. Good agreements between the simulation and the reference are observed for the surface coverage of E(s) and O(s), with the simulated values following the same trends but with slight differences compared to as the reference values. The higher N(s) surface coverage is likely a result of the higher N mass fraction at the wall in the noncatalytic solution from HALO3D. Since the catalytic surface at equilibrium is predominantly populated by E(s) and O(s), accurate predictions of E(s) and O(s) surface coverage are prioritized.

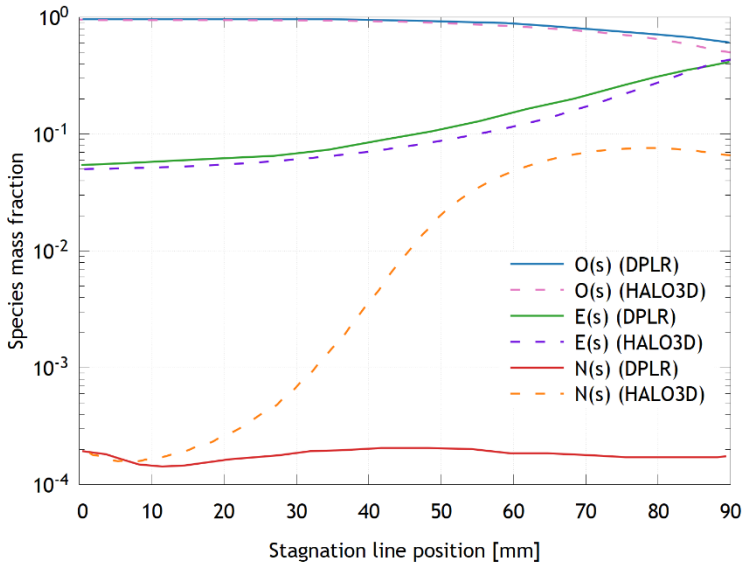

Figure 5.16. Surface coverage of E(s), N(s), and O(s) for the cylinder test case.

The cylinder test case has illustrated the ability of finite-rate surface chemistry model to provide good estimations of the volume and surface species composition on a catalytic surface. Further investigations are required to derive the full setup used by MacLean et al., in order to achieve better agreement with the reference values.

Chapter 6. Conclusion and Future Developments

This thesis presents the development of a gas-surface interaction module within an edge-based finite element multiphysics framework. As a macroscopic description of surface catalycity, the partially catalytic model has been introduced with constant recombination efficiencies derived from arcjet test data. The finite-rate surface chemistry model, a higher-fidelity microscopic approach towards surface catalycity, is also implemented. Surface and bulk species with distinct thermodynamic properties are added to complement existing volume species. Detailed surface reactions are modeled with reaction rate coefficients being dependent on surface properties. Both models interface with the flow and volume chemistry solvers as boundary conditions in terms of species mass and energy.

The verification and validation for the partially catalytic model with constant recombination efficiencies are performed using the Electre test case which involves a five-species Mach 9.7 flow around a blunt cone. Multiple runs with varying recombination efficiency values are conducted to simulate different degrees of surface catalycity. Heat flux profiles with $\gamma_N = \gamma_O = 1$ compare well with the fully catalytic results from Fluent, while predictions for $\gamma_N = \gamma_O = 0.005$ and $\gamma_N = \gamma_O = 0.05$ closely bracket the experimental data from the high-enthalpy shock tunnel of the German Aerospace Center.

The spatial assembly of volume species mass residuals and the temporal integration of surface species concentrations for the finite-rate surface chemistry model are validated using a zero-dimensional reactor. One irreversible adsorption reaction N + E(s) → N(s) with known reaction rate coefficient parameters is present in the test case. The fixed N concentration and simplified reaction kinetics reduce the system to a first order ODE and allow an analytical solution to be derived. The transient response of N(s) surface coverage completely matches the analytical expression.

The computation of forward and backward surface reaction rate coefficients for the finite-rate surface chemistry model is verified using a zero-dimensional reactor. The test case

consists of reversible AD, ER, and LH surface reactions with known reaction rate coefficient parameters for the forward reactions and the backward AD reaction. Equilibrium constants and backward reaction rate for non-AD reactions are obtained using a workaround. The surface coverage of O(s) and the loss efficiencies of O and O_2 calculated from the surface reaction rate coefficients exhibit excellent agreement with the numerical results from Marschall et al., signifying the accurate characterization of all reaction rate coefficients and the correct implementation of the workaround.

The added ability by this thesis to HALO3D for forecasting the volume and surface species composition at the wall is demonstrated through a steady-state test case of a reacting air flow around a two-dimensional cylinder with a catalytic silica surface. The test case employs the Park's 1993 volume chemistry model and the air and silica system of surface reactions. The catalytic solution is computed by restarting from the noncatalytic solution and imposing the finite-rate surface chemistry boundary condition. The species mass fraction of N, O, and NO along the stagnation line and the surface coverage of E(s), N(s), and O(s) for the catalytic solution show good agreement with the DPLR results.

The capability to handle highly stretched meshes is an inherent and unique feature of edge-based FEM that enables the incorporation of an anisotropic mesh optimizer into the solution strategy. The use of OptiGrid in conjunction with an unstructured mesh for the Electre test case has showcased its ability to directionally refine the grid and automatically align element edges with singular flow phenomena. The discontinuity of the shock is much better resolved with the adapted unstructured mesh compared to the structured grid, contributing to a more accurate surface heat flux estimation, and demonstrating that anisotropic mesh optimization is indispensable for aerothermal simulations involving complex three-dimensional geometries.

This work is a part of a continuous effort to augment the capabilities of HALO3D, a comprehensive software that can simulate the aerothermal conditions along the entire trajectory of a hypersonic reentry vehicle. The recent expansion of the volume chemistry solver into the weakly ionized regime opens the possibility for surface reactions involving

ionized species. The development of the ablation module is underway separately to model the transient thermal behavior and surface recession of ablative TPS in response to the wall heat flux calculated by the flow and volume chemistry solvers together with the gas-surface interaction module. The provisioning for other surface reaction mechanisms such as sublimation/deposition, oxidation/reduction, and surface nitrification would permit the modeling of non-charring and charring ablators. Finally, the inclusion of momentum conservations at the surface would allow for the incorporation of transpiration cooling as an active heat rejection technique in reusable TPS designs.

References

[1] Zuppardi, G. and Verde, G., "An Approximate Method to Evaluate the Surface Catalycity in High-Enthalpy Flows," *Transactions on Modelling and Simulation*, vol. 16, no. 1, pp. 589–598, 1997.

[2] Miller, J. H., Tannehill, J. C., Wadawadigi, G., Edwards, T. A., and Lawrence, S. L., "Computation of Hypersonic Flows with Finite Catalytic Walls," *Journal of Thermophysics and Heat Transfer*, vol. 9, no. 3, pp. 486–493, 1995.

[3] Valentini, P., Schwartzentruber, T. E., and Cozmuta, I., "A Mechanism-Based Finite-Rate Surface Catalysis Model for Simulating Reacting Flows," *Journal of Heat Transfer*, vol. 117, no. 1, pp. 495–501, 2009.

[4] Marschall, J. and MacLean, M., "Finite-Rate Surface Chemistry Model, I: Formulation and Reaction System Examples," AIAA Paper 2011-3783, 2011.

[5] MacLean, M., Marschall, J., and Driver D. M., "Finite-Rate Surface Chemistry Model, II: Coupling to Viscous Navier–Stokes Code," AIAA Paper 2011-3784, 2011.

[6] Alkandry, H., Farbar, E., and Boyd, I. D., "Evaluation of Finite-Rate Surface Chemistry Models for Simulation of the Stardust Reentry Capsule," AIAA Paper 2012-2874, 2012.

[7] Sorensen, C., Valentini, P., and Schwartzentruber, T. E., "Uncertainty Analysis of Reaction Rates in a Finite-Rate Surface Catalysis Model," *Journal of Thermophysics and Heat Transfer*, vol. 26, no. 3, pp. 407–416, 2012.

[8] Gao, S., Habashi, W. G., Isola, D., Baruzzi, G. S., and Fossati, M., "A Jacobian-Free Edge-Based Galerkin Formulation for Compressible Flows," *Computers & Fluids*, vol. 143, no. 1, pp. 141–156, 2016.

[9] Seguin, J., Gao, S., Habashi, W. G., Isola, D., and Baruzzi, G. S., "A Finite Element Solver for Hypersonic Flows in Thermo-Chemical Nonequilibrium, Part I," *International Journal of Numerical Methods for Heat & Fluid Flow*, vol. 29, no. 7, pp. 2352–2388, 2019.

[10] Dumas, M.-E., Habashi, W. G., Baruzzi, G. S., Isola, D., and Fossati, M., "Finite Element Modeling of Nonequilibrium Fluid-Wall Interaction at High-Mach Regime," *Journal of Aircraft*, vol. 54, no. 6, pp. 2330–2339, 2017.

[11] Zhang, W., Habashi, W. G., Salah, N. B., Isola, D., and Baruzzi, G. S., "Edge-Based Finite Element Formulation of Hypersonic Flows under an Imposed Magnetic Field," *AIAA Journal*, vol. 56, no. 7, pp. 2756–2768, 2018.

[12] Zhang, W., Habashi, W. G., Salah, N. B., Isola, D., and Baruzzi, G. S., "Edge-Based Finite Element Modeling of Magnetogasdynamic-Based Propulsion Systems," *AIAA Journal*, vol. 57, no. 7, pp. 3003–3013, 2019.

[13] Shrutakeerti, M. V., Casseau, V., Habashi, W. G., and Karchani, A., "Automatic Mesh Optimization of Direct Simulation Monte Carlo Methods for Hypersonic Flows," *65th CASI Aeronautics Conference*, Virtual Online, 14–18 June 2021.

[14] Anderson, J. D., *Fundamentals of Aerodynamics*, 5th ed., McGraw Hill, New York, NY, USA, 2011.

[15] Whitcomb, R. T., "A Study of the Zero Lift Drag Rise Characteristics of Wing Body Combinations near the Speed of Sound," NASA NTRS 19930092271, 1956.

[16] Bianchi, D., "Modeling of Ablation Phenomena in Space Applications," Ph.D. thesis, Dept. Mech. & Aeronaut. Eng., Roma La Sapienza Univ., Rome, Italy, 2007.

[17] Casseau, V., "An Open-Source CFD Solver for Planetary Entry," Ph.D. thesis, Dept. Mech. & Aerosp. Eng., Univ. Strathclyde, Glasgow, UK, 2017.

[18] Bird, G. A., *Molecular Gas Dynamics and the Direct Simulation of Gas Flows*, Clarendon Press, Oxford, UK, 1994

[19] Palharini, R. C., "Atmospheric Reentry Modelling using an Open-Source DSMC Code," Ph.D. thesis, Dept. Mech. & Aerosp. Eng., Univ. Strathclyde, Glasgow, UK, 2014.

[20] Harvey, G. A., "Simulated Reentry Heating by Torching," NASA NTRS 20080042413, 2008.

[21] Trumble, K. A., Cozmuta, I., Sepka, S., Jenniskens, P., and Winter, M., "Postflight Aerothermal Analysis of Stardust Sample Return Capsule," *Journal of Spacecraft and Rockets*, vol. 47, no. 5, pp. 765–774, 2010.

[22] Laub, B. and Venkatapathy, E., "Thermal Protection System Technology and Facility Needs for Demanding Future Planetary Missions," in *Proceedings of the International Workshop Planetary Probe Atmospheric Entry and Descent Trajectory Analysis and Science*, ESA SP-544, Lisbon, Portugal, 6–9 October 2003, Wilson, A., Ed., pp. 239–247, ESA Publications Division, Noordwijk, Netherlands, 2004.

[23] Burnett, D. S., Barraclough, B. L., Bennett, R., Neugebauer, M., Oldham, L. P., Sasaki, C. N., Sevilla, D., Smith, N., Stansbery, E., Sweetnam, D., and Wiens, R. C., "The Genesis Discovery Mission Return of Solar Matter to Earth," *Space Science Reviews*, vol. 105, no. 1, pp. 509–534, 2003.

[24] Pavlosky, J. E. and St. Leger, L. G., "Apollo Experience Report - Thermal Protection Subsystem," NASA NTRS 19740007423, 1974.

[25] Willcockson, W. H., "Stardust Sample Return Capsule Design Experience," *Journal of Spacecraft and Rockets*, vol. 36, no. 3, pp. 770–774, 1999.

[26] Beck, R. A. S., Driver, D. M., Wright, M. J., Hwang, H. H., Edquist, K. T., and Sepka, S. A., "Development of the Mars Science Laboratory Heatshield Thermal Protection System," *Journal of Spacecraft and Rockets*, vol. 51, no. 4, pp. 1139–1150, 2014.

[27] Anna, A., "Numerical Modeling of Surface Chemistry Processes for Hypersonic Entry Environments," Ph.D. thesis, Dept. Aerosp. Eng., Univ. Michigan, Ann Arbor, MI, USA, 2017.

[28] Curry, D. M., "Space Shuttle Orbiter Thermal Protection System Design and Flight Experience," NASA NTRS 19930023009, 1993.

[29] White, T., Hwang, H. H., Ellerby, D., Gasch, M., Beck, R. A. S., Vander Kam, J., and Venkatapathy, E., "Thermal Protection System Materials for Sample Return Missions," *Bulletin of the American Astronomical Society*, vol. 53, no. 4, pp. 1–8, 2021.

[30] Borrelli, R. and Martucci, A., "SCIROCCO Plasma Wind Tunnel: Synergy between Numerical and Experimental Activities for Tests on Aerospace Structures," in *Wind Tunnels and Experimental Fluid Dynamics Research*, Lerner, J. C. and Boldes, U., Ed., ch. 29, pp. 585–606, IntechOpen, London, UK, 2011.

[31] Grinstead, J. H., "High-Enthalpy Test Methodologies for Thermal Protection Systems Development at NASA Ames Research Center," AIAA Paper 2005-3326, 2005.

[32] Goulard, R., "On Catalytic Recombination Rates in Hypersonic Stagnation Heat Transfer," *Jet Propulsion*, vol. 28, no. 1, pp. 737–745, 1958.

[33] Tong, H., Morse, H. L., and Curry, D. M., "Nonequilibrium Viscous Layer Computations of Space Shuttle TPS Requirements," *Journal of Spacecraft*, vol. 12, no. 12, pp. 739–743, 1975.

[34] Scott, C. D., "Catalytic Recombination of Nitrogen and Oxygen on High-Temperature Reusable Surface Insulation," AIAA Paper 1980-1477, 1980.

[35] Kolodziej, P. and Stewart, D. A., "Nitrogen Recombination on High-Temperature Reusable Surface Insulation and the Analysis of its Effect on Surface Catalysis," AIAA Paper 1987-1637, 1987.

[36] Barbato, M., Giordano, D., and Bruno, C., "Comparison between Finite Rate and Other Catalytic Boundary Conditions for Hypersonic Flows," AIAA Paper 1994-2074, 1994.

[37] Langmuir, I., "The Adsorption of Gasses on Plane Surfaces of Glass, Mica and Platinum," *Journal of American Chemical Society*, vol. 40, no. 9, pp. 1361–1403, 1918.

[38] Langmuir, I., "Chemical Reactions on Surfaces," *Transactions of Faraday Society*, vol. 17, no. 1, pp. 607–620, 1922.

[39] Hinshelwood, C. N., "On the Theory of Unimolecular Reactions," *Proceedings of the Royal Society of London*, vol. 113, no. 1, pp. 230–233, 1926.

[40] Eley, D. D. and Rideal, E. K., "The Catalysis of the Parahydrogen Conversion by Tungsten," *Proceedings of the Royal Society of London*, vol. 178, no. 1, pp. 429–451, 1941.

[41] Deutschmann, O., Riedel, U., and Warnatz, J., "Modelling of Nitrogen and Oxygen Recombination on Partial Catalytic Surfaces," *Journal of Heat Transfer*, vol. 117, no. 1, pp. 495–501, 1995.

[42] Thömel, J., Lukkien, J. J., and Chazot, O., "A Multiscale Approach for Building a Mechanism-Based Catalysis Model for High-Enthalpy Carbon Dioxide Flow," AIAA Paper 2007-4399, 2007.

[43] Thompson, R. A. and Gnoffo, P. A., "Implementation of a Blowing Boundary Condition in the LAURA Code," AIAA Paper 2008-1243, 2008.

[44] Driver, D. M. and MacLean, M., "Improved Predictions of PICA Recession in Arc Jet Shear Tests," AIAA Paper 2011-141, 2011.

[45] Farbar, E., Alkandry, H., Wiebenga, J., and Boyd, I. D., "Simulation of Ablating Hypersonic Vehicles with Finite-Rate Surface Chemistry," AIAA Paper 2014-2124, 2014.

[46] Nag, P. K., *Engineering Thermodynamics*, McGraw Hill, New York, NY, USA, 2002.

[47] McBride, B. J., Zehe, M. J., and Gordon, S., "NASA Glenn Coefficients for Calculating Thermodynamic Properties of Individual Species," NASA NTRS 20020085330, 2002.

[48] Wilke, C. R., "A Viscosity Equation for Gas Mixtures," *Journal of Chemical Physics*, vol. 18, no. 4, pp. 517–519, 1950.

[49] Blottner, F. G., Johnson, M., and Ellis, M., "Chemically Reacting Viscous Flow Program for Multi-Component Gas Mixtures," *Sandia Laboratories*, SC-RR-70-754, 1971.

[50] Vincenti, W. G. and Kruger, C. H., *Introduction to Physical Gas Dynamics*, Krieger, Malabar, FL, USA, 2002.

[51] Fick, A., "Über Diffusion," *Annalen der Physik*, vol. 170, no. 1, pp. 59–86, 1855.

[52] Alkandry, H., Boyd, I. D., and Martin, A., "Comparison of Models for Mixture Transport Properties for Numerical Simulations of Ablative Heat-Shields," AIAA Paper 2013-0303, 2013.

[53] Gosse, R. and Candler, G., "Diffusion Flux Modeling: Application to Direct Entry Problems," AIAA Paper 2005-389, 2005.

[54] Hutton, D. V., *Fundamentals of Finite Element Analysis*, McGraw Hill, New York, NY, USA, 2004.

[55] Luo, H., Baum, J. D., and Lohner, R., "Edge-Based Finite Element Scheme for the Euler Equations," *AIAA Journal*, vol. 32, no. 6, pp. 1183–1190, 1994.

[56] Roe, P. L., "Approximate Riemann Solvers, Parameter Vectors, and Difference Schemes," *Journal of Computational Physics*, vol. 43, no. 2, pp. 357–372, 1981.

[57] Courant, R., Friedrichs, K., and Lewy, H., "Über die Partiellen Differenzengleichungen der Mathematischen Physik," *Mathematische Annalen*, vol. 100, no. 1, pp. 32–74, 1928.

[58] Gear, C. W., *Numerical Initial Value Problems in Ordinary Differential Equations*, Prentice Hall, Englewood Cliffs, NJ, USA, 1971.

[59] Habashi, W. G., Dompierre, J., Bourgault, Y., Fortin, M., and Vallet, M.-G., "Certifiable Computational Fluid Dynamics through Mesh Optimization, Special Issue on Credible Computational Fluid Dynamics Simulation", *AIAA Journal*, vol. 36, no. 5, pp. 703–711, 1998.

[60] Gao, S., Seguin, J., Habashi, W. G., Isola, D., and Baruzzi, G. S., "A Finite Element Solver for Hypersonic Flows in Thermo-Chemical Nonequilibrium, Part II," *International Journal of Numerical Methods for Heat & Fluid Flow*, vol. 30, no. 2, pp. 575–606, 2019.

[61] Maxwell, J. C., "V. Illustrations of the Dynamical Theory of Gases. Part I. On the Motions and Collisions of Perfectly Elastic Spheres," *The London, Edinburgh, and Dublin Philosophical Magazine and Journal of Science*, vol. 19, no. 124, pp. 19–32, 1860.

[62] Guerra, V., "Analytical Model of Heterogeneous Atomic Recombination on Silica-Like Surfaces," *IEEE Transactions on Plasma Science*, vol. 35, no. 5, pp. 1397–1412, 2007.

[63] Walpot, L. and Kordulla, W., "Synthesis of Flow Simulations for Test Case 2.b, Electre Model in the Hypersonic Impulse Facility HEG," ESA HT-TR-E-34-604-DLRG, 1996.

[64] Sagnier, P. and Vérant, J.-L., "Flow Characterization in the ONERA F4 High-Enthalpy Wind Tunnel," *AIAA Journal*, vol. 36, no. 4, pp. 522–531, 1998.

[65] Muylaert, J., Walpot, L., and Vennemann, D., "A Review of European Code-Validation Studies in High-Enthalpy Flow," *Philosophical Transactions of the Royal Society of London. Series A: Mathematical, Physical and Engineering Sciences*, vol. 357, no. 1759, pp. 2249–2278, 1999.

[66] Viviani, A. and Pezzella, G., "Nonequilibrium Aerothermodynamics for a Capsule Reentry Vehicle," *Engineering Applications of Computational Fluid Mechanics*, vol. 3, no. 4, pp. 543–561, 2009.

[67] van Albada, G. D., van Leer, B., and Roberts, W. W., "A Comparative Study of Computational Methods in Cosmic Gas Dynamic," *Astronomy and Astrophysics*, vol. 108, no. 1, pp. 76–84, 1982.

[68] Hollis, B. R. and Collier, A. S, "Turbulent Aeroheating Testing of Mars Science Laboratory Entry Vehicle," *Journal of Spacecraft and Rockets*, vol. 45, no. 3, pp. 417–427, 2008.

[69] Park, C., "Review of Chemical-Kinetic Problems of Future NASA Missions, I: Earth Entries," *Journal of Thermophysics and Heat Transfer*, vol. 7, no. 3, pp. 385–398, 1993.

[70] Dompierre, J., Vallet, M.-G., Bourgault, Y., Fortin, M., and Habashi, W. G., "Anisotropic Mesh Adaptation: towards User-Independent, Mesh-Independent, and Solver-Independent CFD, Part III: Unstructured Meshes," *International Journal for Numerical Methods in Fluids*, vol. 39, no. 8, pp. 675–702, 2002.

[71] Wright, R. L. and Zoby, E. V., "Flight Boundary Layer Transition Measurements on a Slender Cone at Mach 20," AIAA Paper 1977-719, 1977.

A. Appendix

A.1. Species properties

Table A.1. NASA Glenn species properties.

Species	M_s [g/mol]	$h_s^{0,T_{\mathrm{ref}}}$ [J/kg]
N	14.0067400	3.36E+07
O	15.9994000	1.54E+07
N_2	28.0134800	0
O_2	31.9988000	0
NO	30.0061400	3.00E+06

Table A.2. Blottner's curve fit for species viscosity.

$$\mu_s(T) = 0.1 \exp[(A_s \ln(T) + B_s) \ln(T) + C_s]$$

Species	A_s	B_s	C_s
N	1.16E-02	6.03E-01	-1.24E+01
O	2.03E-02	4.29E-01	-1.16E+01
N_2	2.68E-02	3.18E-01	-1.13E+01
O_2	4.49E-02	-8.26E-02	-9.20E+00
NO	4.36E-02	-3.36E-02	-9.58E+00

Table A.3. NASA Glenn thermodynamic model.

$$\frac{c_{\mathrm{p},s}(T)}{R/M_s} = a_1 T^{-2} + a_2 T^{-1} + a_3 + a_4 T + a_5 T^2 + a_6 T^3 + a_7 T^4$$

$$\frac{h_s^0(T)}{RT/M_s} = -a_1 T^{-2} + a_2 \ln(T)\, T^{-1} + a_3 + \frac{1}{2} a_4 T + \frac{1}{3} a_5 T^2 + \frac{1}{4} a_6 T^3 + \frac{1}{5} a_7 T^4 + b_1 T^{-1}$$

$$\frac{s_s^0(T)}{RT/M_s} = -\frac{1}{2} a_1 T^{-2} - a_2 T^{-1} + a_3 \ln(T) + a_4 T + \frac{1}{2} a_5 T^2 + \frac{1}{3} a_6 T^3 + \frac{1}{4} a_7 T^4 + b_2$$

(a) 200 K ≤ T ≤ 1000 K

Species	a_1	a_2	a_3	a_4	a_5	a_6	a_7	b_1	b_2
N	0.00E+00	0.00E+00	2.50E+00	0.00E+00	0.00E+00	0.00E+00	0.00E+00	5.61E+04	4.19E+00
O	-7.95E+03	1.61E+02	1.97E+00	1.01E-03	-1.11E-06	6.52E-10	-1.58E-13	2.84E+04	8.40E+00
N_2	2.21E+04	-3.82E+02	6.08E+00	-8.53E-03	1.38E-05	-9.63E-09	2.52E-12	7.11E+02	-1.08E+01
O_2	-3.43E+04	4.85E+02	1.12E+00	4.29E-03	-6.84E-07	-2.02E-09	1.04E-12	-3.39E+03	1.85E+01
NO	-1.14E+04	1.54E+02	3.43E+00	-2.67E-03	8.48E-06	-7.69E-09	2.39E-12	9.10E+03	6.73E+00

(b) 1000 K ≤ T ≤ 6000 K

Species	a_1	a_2	a_3	a_4	a_5	a_6	a_7	b_1	b_2
N	8.88E+04	-1.07E+02	2.36E+00	2.92E-04	-1.73E-07	4.01E-11	2.68E-15	5.70E+04	4.87E+00
O	2.62E+05	-7.30E+02	3.32E+00	-4.28E-04	1.04E-07	-9.44E-12	2.73E-16	3.39E+04	-6.68E-01
N_2	5.88E+05	-2.24E+03	6.07E+00	-6.14E-04	1.49E-07	-1.92E-11	1.06E-15	1.28E+04	-1.59E+01
O_2	-1.04E+06	2.34E+03	1.82E+00	1.27E-03	-2.19E-07	2.05E-11	-8.19E-16	-1.69E+04	1.74E+01
NO	2.24E+05	-1.29E+03	5.43E+00	-3.66E-04	9.88E-08	-1.42E-11	9.38E-16	1.75E+04	-8.50E+00

(c) 6000 K ≤ T ≤ 20000 K

Species	a_1	a_2	a_3	a_4	a_5	a_6	a_7	b_1	b_2
N	5.48E+08	-3.11E+05	6.92E+01	-6.85E-03	3.83E-07	-1.10E-11	1.28E-16	2.55E+06	-5.85E+02
O	1.78E+08	-1.08E+05	2.81E+01	-2.98E-03	1.85E-07	-5.80E-12	7.19E-17	8.89E+05	-2.18E+02
N_2	8.31E+08	-6.42E+05	2.02E+02	-3.07E-02	2.49E-06	-9.71E-11	1.44E-15	4.94E+06	-1.67E+03
O_2	4.98E+08	-2.87E+05	6.69E+01	-6.17E-03	3.02E-07	-7.42E-12	7.28E-17	2.29E+06	-5.53E+02
NO	-9.58E+08	5.91E+05	-1.38E+02	1.69E-02	-1.01E-06	2.91E-11	-3.30E-16	-4.68E+06	1.24E+03

A.2. Volume chemistry model

Table A.4. Park's 1993 reaction model.

Reaction	M	C_r	β_r	$T_{c,r}$ [K]
$N_2 + M \rightleftharpoons 2N + M$	N, O	3.0E+22	-1.6	113200
	N_2, O_2, NO	7.0E+21	-1.6	113200
$N_2 + M \rightleftharpoons 2N + M$	N, O	1.0E+22	-1.6	59500
	N_2, O_2, NO	2.0E+21	-1.6	59500
$NO + M \rightleftharpoons N + O + M$	N, O	1.1E+17	0	75500
	N_2, O_2, NO	5.0E+15	0	75500
$N_2 + O \rightleftharpoons NO + N$	-	6.4E+17	-1.0	38400
$NO + O \rightleftharpoons O_2 + N$	-	8.4E+12	0	19450

A.3. Reactor results

Table A.5. Gibbs free energies of O, O_2, and O(s).

T [K]	O	O_2	O(s)	$-\ln(K_{a,AD})RT$
500	1.674186E+05	-1.042634E+05	-1.396310E+05	-3.070495E+05
600	1.500002E+05	-1.266284E+05	-1.480050E+05	-2.980052E+05
700	1.322278E+05	-1.495300E+05	-1.566634E+05	-2.888913E+05
800	1.141535E+05	-1.729040E+05	-1.655642E+05	-2.797177E+05
900	9.581616E+04	-1.967007E+05	-1.746759E+05	-2.704921E+05
1000	7.724531E+04	-2.208796E+05	-1.839749E+05	-2.612202E+05
1100	5.846539E+04	-2.454076E+05	-1.934412E+05	-2.519066E+05
1200	3.949515E+04	-2.702564E+05	-2.030601E+05	-2.425552E+05
1300	2.035062E+04	-2.954019E+05	-2.128185E+05	-2.331691E+05
1400	1.045372E+03	-3.208237E+05	-2.227057E+05	-2.237510E+05
1500	-1.840901E+04	-3.465044E+05	-2.327122E+05	-2.143032E+05
1600	-3.800249E+04	-3.724285E+05	-2.428302E+05	-2.048277E+05
1700	-5.772631E+04	-3.985828E+05	-2.530524E+05	-1.953261E+05
1800	-7.757273E+04	-4.249553E+05	-2.633728E+05	-1.858001E+05
1900	-9.753491E+04	-4.515353E+05	-2.737859E+05	-1.762509E+05
2000	-1.176067E+05	-4.783133E+05	-2.842867E+05	-1.666799E+05
2100	-1.377827E+05	-5.052807E+05	-2.948708E+05	-1.570881E+05
2200	-1.580579E+05	-5.324296E+05	-3.055344E+05	-1.474765E+05
2300	-1.784277E+05	-5.597527E+05	-3.162737E+05	-1.378460E+05
2400	-1.988882E+05	-5.872435E+05	-3.270856E+05	-1.281974E+05
2500	-2.194355E+05	-6.148960E+05	-3.379670E+05	-1.185314E+05
2600	-2.400663E+05	-6.427045E+05	-3.489152E+05	-1.088489E+05
2700	-2.607773E+05	-6.706639E+05	-3.599276E+05	-9.915031E+04
2800	-2.815657E+05	-6.987692E+05	-3.710020E+05	-8.943636E+04
2900	-3.024287E+05	-7.270160E+05	-3.821363E+05	-7.970755E+04
3000	-3.233639E+05	-7.554002E+05	-3.933283E+05	-6.996440E+04
3100	-3.443689E+05	-7.839176E+05	-4.045763E+05	-6.020739E+04
3200	-3.654416E+05	-8.125647E+05	-4.158786E+05	-5.043698E+04
3300	-3.865799E+05	-8.413379E+05	-4.272335E+05	-4.065356E+04
3400	-4.077819E+05	-8.702339E+05	-4.386395E+05	-3.085755E+04
3500	-4.290459E+05	-8.992497E+05	-4.500952E+05	-2.104931E+04

Table A.6. Reaction rate coefficients and equilibrium constants for reversible AD reaction.

T [K]	$k_{\mathrm{f,AD}}$	$k_{\mathrm{b,AD}}$	$K_{\mathrm{c,AD}}$
500	1.355717E+06	3.114482E+03	8.266621E-16
600	1.485114E+06	4.893414E+03	1.514688E-10
700	1.604106E+06	6.838611E+03	8.806427E-07
800	1.714861E+06	8.869022E+03	5.916272E-04
900	1.818885E+06	1.093243E+04	9.419827E-02
1000	1.917273E+06	1.299593E+04	5.470871E+00
1100	2.010853E+06	1.503912E+04	1.525168E+02
1200	2.100268E+06	1.704966E+04	2.451034E+03
1300	2.186028E+06	1.902038E+04	2.577694E+04
1400	2.268549E+06	2.094742E+04	1.942336E+05
1500	2.348171E+06	2.282909E+04	1.120745E+06
1600	2.425180E+06	2.466507E+04	5.205310E+06
1700	2.499819E+06	2.645592E+04	2.021724E+07
1800	2.572292E+06	2.820272E+04	6.764444E+07
1900	2.642779E+06	2.990691E+04	1.996025E+08
2000	2.711434E+06	3.157008E+04	5.292712E+08
2100	2.778393E+06	3.319393E+04	1.280481E+09
2200	2.843776E+06	3.478015E+04	2.861917E+09
2300	2.907689E+06	3.633045E+04	5.970320E+09
2400	2.970227E+06	3.784646E+04	1.172519E+10
2500	3.031475E+06	3.932977E+04	2.183507E+10
2600	3.091510E+06	4.078189E+04	3.879283E+10
2700	3.150402E+06	4.220427E+04	6.609508E+10
2800	3.208212E+06	4.359827E+04	1.084786E+11
2900	3.264999E+06	4.496517E+04	1.721659E+11
3000	3.320815E+06	4.630620E+04	2.651100E+11
3100	3.375708E+06	4.762249E+04	3.972311E+11
3200	3.429723E+06	4.891513E+04	5.806351E+11
3300	3.482900E+06	5.018513E+04	8.298076E+11
3400	3.535278E+06	5.143345E+04	1.161778E+12
3500	3.586890E+06	5.266099E+04	1.596247E+12

Table A.7. Reaction rate coefficients and equilibrium constants for reversible ER reaction.

T [K]	$k_{\mathrm{f,ER}}$	$k_{\mathrm{b,ER}}$	$K_{\mathrm{c,ER}}$
500	2.733679E-25	4.993185E-11	6.572663E+01
600	3.393306E-19	3.105618E-08	4.207227E+03
700	7.645240E-15	3.165851E-06	8.553902E+04
800	1.405941E-11	1.035924E-04	8.428730E+05
900	4.864990E-09	1.583215E-03	5.100224E+06
1000	5.228460E-07	1.416906E-02	2.187259E+07
1100	2.400711E-05	8.577445E-02	7.286076E+07
1200	5.825209E-04	3.869441E-01	2.005603E+08
1300	8.653875E-03	1.391110E+00	4.762322E+08
1400	8.743706E-02	4.181866E+00	1.006043E+09
1500	6.490067E-01	1.088976E+01	1.934269E+09
1600	3.749589E+00	2.522562E+01	3.443234E+09
1700	1.762391E+01	5.304984E+01	5.750284E+09
1800	6.974948E+01	1.029056E+02	9.102473E+09
1900	2.388314E+02	1.864502E+02	1.376977E+10
2000	7.230809E+02	3.187354E+02	2.003756E+10
2100	1.969989E+03	5.183122E+02	2.819915E+10
2200	4.899705E+03	8.071562E+02	3.854860E+10
2300	1.125815E+04	1.210429E+03	5.137445E+10
2400	2.413547E+04	1.756101E+03	6.695425E+10
2500	4.867988E+04	2.474477E+03	8.555022E+10
2600	9.302620E+04	3.397648E+03	1.074058E+11
2700	1.694444E+05	4.558916E+03	1.327434E+11
2800	2.956976E+05	5.992210E+03	1.617623E+11
2900	4.965820E+05	7.731529E+03	1.946383E+11
3000	8.056095E+05	9.810418E+03	2.315232E+11
3100	1.266780E+06	1.226150E+04	2.725452E+11
3200	1.936385E+06	1.511608E+04	3.178091E+11
3300	2.884784E+06	1.840376E+04	3.673980E+11
3400	4.198084E+06	2.215223E+04	4.213737E+11
3500	5.979684E+06	2.638699E+04	4.797785E+11

Table A.8. Reaction rate coefficients and equilibrium constants for reversible LH reaction.

T [K]	$k_{\mathrm{f,LH}}$	$k_{\mathrm{b,LH}}$	$K_{\mathrm{c,LH}}$
500	4.959313E+30	6.237465E+13	1.257728E-17
600	4.376598E+24	1.575665E+11	3.600205E-14
700	2.098176E+20	2.160118E+09	1.029522E-11
800	1.219725E+17	8.561459E+07	7.019173E-10
900	3.738723E+14	6.905211E+06	1.846944E-08
1000	3.666995E+12	9.172051E+05	2.501245E-07
1100	8.376076E+10	1.753334E+05	2.093264E-06
1200	3.605481E+09	4.406234E+04	1.222093E-05
1300	2.526069E+08	1.367281E+04	5.412682E-05
1400	2.594493E+07	5.009107E+03	1.930669E-04
1500	3.618099E+06	2.096381E+03	5.794151E-04
1600	6.467857E+05	9.777784E+02	1.511750E-03
1700	1.418425E+05	4.986993E+02	3.515867E-03
1800	3.687901E+04	2.740640E+02	7.431435E-03
1900	1.106546E+04	1.604016E+02	1.449571E-02
2000	3.749835E+03	9.904795E+01	2.641395E-02
2100	1.410360E+03	6.404234E+01	4.540851E-02
2200	5.803974E+02	4.308974E+01	7.424178E-02
2300	2.582742E+02	3.001453E+01	1.162119E-01
2400	1.230648E+02	2.155142E+01	1.751225E-01
2500	6.227368E+01	1.589418E+01	2.552310E-01
2600	3.323268E+01	1.200298E+01	3.611799E-01
2700	1.859253E+01	9.257524E+00	4.979162E-01
2800	1.084964E+01	7.275825E+00	6.706053E-01
2900	6.574944E+00	5.815819E+00	8.845427E-01
3000	4.122115E+00	4.720105E+00	1.145069E+00
3100	2.664794E+00	3.883904E+00	1.457487E+00
3200	1.771198E+00	3.235967E+00	1.826993E+00
3300	1.207335E+00	2.726895E+00	2.258607E+00
3400	8.421169E-01	2.321818E+00	2.757121E+00
3500	5.998461E-01	1.995718E+00	3.327050E+00

Table A.9. Surface concentrations of O(s) with reversible AD, ER, and LH reactions.

T [K]	p = 200 Pa	p = 2000 Pa	p = 20000 Pa
500	7.482810E-06	7.482810E-06	7.482810E-06
600	7.475369E-06	7.475369E-06	7.475369E-06
700	7.468162E-06	7.468162E-06	7.468162E-06
800	7.461411E-06	7.461411E-06	7.461411E-06
900	7.455191E-06	7.455191E-06	7.455191E-06
1000	7.449505E-06	7.449505E-06	7.449505E-06
1100	7.444322E-06	7.444326E-06	7.444326E-06
1200	7.439548E-06	7.439606E-06	7.439612E-06
1300	7.434609E-06	7.435252E-06	7.435316E-06
1400	7.425814E-06	7.430857E-06	7.431362E-06
1500	7.394458E-06	7.424497E-06	7.427529E-06
1600	7.269103E-06	7.408443E-06	7.423014E-06
1700	6.870078E-06	7.357457E-06	7.415183E-06
1800	6.023304E-06	7.207461E-06	7.396589E-06
1900	4.887475E-06	6.852890E-06	7.349363E-06
2000	3.789534E-06	6.238650E-06	7.238914E-06
2100	2.884465E-06	5.460580E-06	7.019248E-06
2200	2.182190E-06	4.666180E-06	6.666762E-06
2300	1.647037E-06	3.940098E-06	6.210990E-06
2400	1.240376E-06	3.308045E-06	5.708723E-06
2500	9.311965E-07	2.768919E-06	5.204011E-06
2600	6.964421E-07	2.312902E-06	4.719976E-06
2700	5.190658E-07	1.928575E-06	4.266438E-06
2800	3.861034E-07	1.605299E-06	3.846742E-06
2900	2.873398E-07	1.333837E-06	3.461314E-06
3000	2.145644E-07	1.106367E-06	3.109239E-06
3100	1.612099E-07	9.162909E-07	2.788955E-06
3200	1.221430E-07	7.580113E-07	2.498579E-06
3300	9.346698E-08	6.267285E-07	2.236081E-06
3400	7.230126E-08	5.182830E-07	1.999386E-06
3500	5.655708E-08	4.290464E-07	1.786443E-06